# NLO QCD corrections to polarized diboson production in semileptonic final states

Ansgar Denner[*] and Christoph Haitz[†]
*Universität Würzburg, Institut für Theoretische Physik und Astrophysik, 97074 Würzburg, Germany*

Giovanni Pelliccioli[‡]
*Max-Planck-Institut für Physik, Föhringer Ring 6, 80805 München, Germany*

(Received 24 November 2022; accepted 12 February 2023; published 13 March 2023)

Understanding the polarization structure and providing precise predictions for multiboson processes at the LHC is becoming urgent in the light of the upcoming run-3 and high-luminosity data. The CMS and ATLAS collaborations have already started using polarized predictions to perform template fits of the data, getting access to the polarization of W and Z bosons. So far, only fully leptonic decay channels have been considered in this perspective. The natural step forward is the investigation of hadronic decays of electroweak bosons. In this work, we compute NLO QCD corrections to the production and decay of WZ pairs at the LHC in final states with two charged leptons and jets. The calculation relies on the double-pole approximation and the separation of polarized states at the level of Standard Model amplitudes. The presented NLO-accurate results are necessary building blocks for a broad understanding and precise modeling of polarized diboson production in semileptonic decay channels.

DOI: 10.1103/PhysRevD.107.053004

## I. INTRODUCTION

The pioneering measurements with the run-2 LHC dataset in diboson inclusive production [1–3] and scattering (VBS) [4] have paved the way toward a refined experimental investigation of the polarization states of electroweak (EW) bosons produced in multiboson processes. The most striking difference of the methods adopted in Refs. [1–4] with respect to previous polarization analyses [5–11] is the usage of polarized-signal templates directly generated with Monte Carlo generators, which is expected to give a more complete picture of the polarization structure than the simple evaluation of angular coefficients, giving access to interference effects and spin correlations.

The extraction of angular coefficients from unpolarized decay-angle distributions was first proposed in Ref. [12,13] and has been applied in several theoretical studies on $V+\mathrm{j}$ [12–16] and inclusive diboson production [17–21]. The direct Monte Carlo simulation of processes with intermediate EW polarized bosons was proposed for VBS [22–25] and it is currently available in public codes at leading-order (LO) accuracy matched to parton-shower (PS) in the Standard Model (SM) as well as in the presence of beyond-SM effects. The extension of this approach to higher perturbative orders has been carried out focusing on diboson inclusive production, reaching next-to-leading-order (NLO) in the QCD coupling [26,27] and later on NLO in the EW coupling [28–30] and next-to-next-to-leading-order (NNLO) in QCD [31]. Analogous methods have been applied to Higgs decays [32,33] and to $V+\mathrm{j}$ production [34]. A number of works have tackled the polarization structure of VBS with machine-learning techniques with promising results [35–38].

So far, both experimental measurements [1–11] and phenomenological studies [12–37,39–43] have focused on leptonic decays of weak bosons, cleaner than the hadronic ones in a hadron-collider environment, but with a smaller branching ratio and affected by reconstruction effects in the presence of neutrinos in the final state. Indeed, the increasing interest in measuring gauge-boson polarizations at the LHC and the lack of statistics in fully leptonic decay channels has triggered a number of phenomenological studies [44–47] of processes with hadronically decaying bosons. The hadronic decay of W and Z bosons has the great advantage of larger branching ratio with respect to the leptonic one, but the disadvantage of much larger backgrounds to deal with in the LHC environment that is dominated by QCD-induced processes. The focus of these polarization studies has been put especially on the discrimination between longitudinal and transverse bosons in

[*]ansgar.denner@physik.uni-wuerzburg.de
[†]christoph.haitz@physik.uni-wuerzburg.de
[‡]gpellicc@mpp.mpg.de

boosted kinematic configurations [44–46]. The driving idea is that the reconstruction of the boosted-fat-jet substructure, making use of either traditional substructure observables like $N$-subjettiness [44] and soft-drop [46], or machine-learning [45] techniques, is expected to maximize the information about the polarization state of the decayed boson, since the jet constituents can be associated to some degree of precision to the decay quarks. Recently it has been proposed to use energy correlators to improve the polarization discrimination [47]. The existing studies of polarized bosons in the leptonic decay channel suggest that there are LHC observables that enable to discriminate polarization states without the need to reconstruct individual decay products [3].

So far, no polarization measurement has been carried out yet with hadronic decays of gauge bosons, although a number of sensitivity studies have been performed for the high-energy [48] and high-luminosity (HL) [49] runs of the LHC, mostly targeting VBS processes.

In the specific case of inclusive diboson production, the semileptonic decay channel has been investigated with 13-TeV LHC data with the aim of searching for new resonances [50–54]. Measuring polarizations in this channel could further constrain new-physics effects [55] and in particular the spin of possible underlying resonances decaying in two gauge bosons. In spite of the high-precision SM predictions available for unpolarized [56–77] and polarized [26–31] diboson production at the LHC, the fully leptonic decay channel has always been considered and no tailored study beyond LO (+PS) exists for the semileptonic channel in the presence of polarized intermediate bosons. The NLO QCD corrections to the hadronic decay of polarized weak bosons have been known for many years [78,79] and can be generated easily with the help of any one-loop amplitude provider, but they have not been combined yet with realistic LHC production processes.

In this work we perform a consistent combination of NLO QCD corrections to diboson production and to the hadronic decay of one of the two bosons in the double-pole approximation [80,83–87] and in the presence of polarized and unpolarized intermediate bosons, preserving partial off-shell effects and the complete spin correlations between production and decay. This target is pursued following the strategy proposed at LO in Ref. [22] and later extended to NLO in Refs. [26,28,30]. We consider a boosted regime for the weak bosons, where the doubly longitudinal signal is expected to be sizeable [27], but we do not make use of any jet-substructure-reconstruction technique.

This paper is organized as follows. In Sec. II we describe the technical details of the calculation, the SM input parameters and the kinematic setups that are considered. In Sec. III we present and discuss the integrated and differential predictions for doubly polarized signals at the LHC with 13.6-TeV center-of-mass (c.m.) energy. Our conclusions and outlook are given in Sec. IV.

## II. DETAILS OF THE CALCULATION

We consider diboson ($ZW^+$) inclusive production at the LHC:

$$\begin{aligned} pp &\to Z(\to \ell^+\ell^-)W^+(\to jj) + X, \\ pp &\to Z(\to \ell^+\ell^-)W^+(\to J) + X, \end{aligned} \tag{1}$$

where the two semileptonic decay channels differ by the number of jets from the decay of the W boson. In the first case (resolved topology) the $W^+$ boson decays into two light jets, while in the second case (unresolved topology) it decays into a single fat jet. We calculate the NLO QCD corrections to the tree-level EW process, i.e., of perturbative order $\mathcal{O}(\alpha_s\alpha^4)$, working in the double-pole approximation (DPA) [83–87]. The nonresonant contributions and off-shell effects beyond the DPA, as well as the other perturbative orders contributing to the same final state (which cannot embed two weak-boson propagators) are not considered here. In other words, we do not include the irreducible nonresonant and QCD multijet backgrounds to the diboson signal. We also restrict the calculation to $ZW^+$ production, neglecting the $ZW^-$ and ZZ resonant processes which also contribute to the same final state with two leptons and a hadronic system. A rough estimate of the missing resonant contributions ($ZW^-$ and ZZ), of the nonresonant EW effects, and of the QCD background is provided at the end of Sec. III A. Owing to the different resonance and spin structures of the various subprocesses in the SM, it is preferable to investigate doubly polarized signals with LHC data focusing on one resonant structure at a time, i.e., considering other (unpolarized) resonant processes as contributions to be subtracted on equal footing with the QCD irreducible backgrounds and off-shell EW effects. This approach could be beneficial also in the light of possible new-physics effects that may distort the SM dynamics differently for various diboson processes. Therefore, the study of $W^+Z$ production presented here, which is not meant to be fully realistic, is expected to give useful insights for future analyses in semileptonic final states with run-3 and HL-LHC data.

### A. Double-pole approximation and polarized-signal definition

Sample diagrams for $ZW^+$ production that contribute in the DPA at LO and at NLO QCD are shown in Fig. 1. In the DPA [83–87] all diagrams without two $s$-channel boson propagators (one $W^+$ and one Z boson) are neglected, giving an amplitude (which is not gauge invariant) that is fully factorized in a production × decay form. In order to recover the EW gauge invariance, the numerator of the doubly resonant amplitude is evaluated with a modified kinematics obtained via an on-mass-shell projection of the resonant EW bosons, while the denominator (i.e., the two Breit–Wigner distributions from the weak-boson propagators) is evaluated

with the original kinematics (for off-shell bosons). The widths of the W and Z bosons are set to zero in the amplitude numerator, while they are kept finite in the denominators of the weak-boson propagators targeted by the DPA. A detailed explanation of the DPA and the gauge invariance in this formalism can be found in Refs. [26,85,87,88].

This technique preserves all spin correlations (the full spin matrix is accounted for) and partial off-shell effects (thanks to the Breit–Wigner modulation and the use of the off-shell phase space). An alternative method that is often used for polarized-signal simulation [25,31,34] is the narrow-width approximation [89,90]. While in the narrow-width approximation the off-shell effects are neglected, the DPA takes into account off-shell effects partially. Specifically, the phase space and the Breit–Wigner denominators of the resonances are treated off shell, and only the matrix-element numerators are projected on the resonance mass shell.

The DPA approach makes it natural to separate polarization states of intermediate weak bosons at amplitude level [22,26]. A priori, the polarization of particles in scattering processes can only be defined for stable external particles, while for intermediate (virtual) particles it is required to perform the sum over all polarizations (physical and unphysical). The factorized structure of double-pole-approximated, doubly resonant amplitudes enables the splitting of the numerator of each gauge-boson propagator into the sum over physical polarization states: longitudinal (L), left handed (−) and right handed (+). The contributions of unphysical polarization states are exactly cancelled by those of would-be Goldstone bosons on the mass shell. Therefore, replacing the polarization sum in the propagator numerator with the contribution of a specific polarization state $\lambda$ gives a gauge-invariant $\lambda$-polarized amplitude, where $\lambda = 0, \pm$. A convenient choice [23] is to consider the transverse-polarization state (T) which is defined as the coherent sum of the left- and right-handed states, including also the left–right interference term.

It is essential to recall that the polarization vectors appearing in the propagator numerator depend on the Lorentz frame where the kinematics is evaluated. This implies that the definition of the polarized signal is reference-frame dependent. The preferred choice for diboson inclusive production is the diboson–system c.m. frame [1,20,27], as it allows for a natural interpretation in terms of the corresponding tree-level $2 \to 2$ process ($q_u \bar{q}_d \to ZW^+$). This is the choice adopted in this work.

As previously stated, the novel aspect of the presented calculation with respect to Ref. [27] is the semileptonic decay channel [see Eq. (1)]. In the fully leptonic decay channel, the NLO QCD corrections only enter as initial-state virtual and real radiation. Here we also need to consider the NLO QCD corrections to the $W^+$-boson decay. As can be appreciated in Fig. 1, the factorizable virtual corrections to the decay [Fig. 1(c)] and to the production subprocess [Fig. 1(b)] are accounted for. The real corrections include initial-state-radiation [Figs. 1(d) and 1(e)] and final-state-radiation [Fig. 1(f)] contributions. Both virtual and real nonfactorizable NLO QCD corrections to doubly resonant amplitudes (gluon exchange between production and decay) vanish owing to color algebra.

The treatment of factorizable real QCD corrections in the DPA is carried out using the general approach introduced in

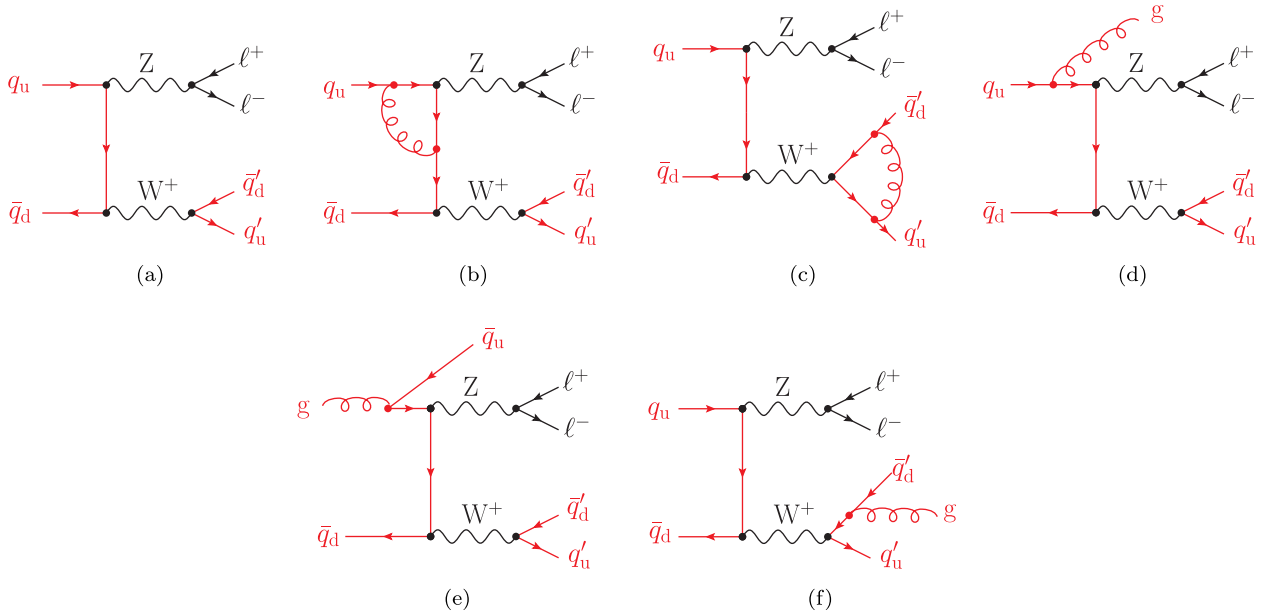


FIG. 1. Sample tree-level (a), one-loop (b, c), and real-radiation (d–f) diagrams contributing to diboson production at the LHC in the semileptonic decay channel at NLO QCD. Particles carrying color charge are highlighted in red.

Refs. [28,91–93] for NLO EW corrections, upon the replacement of the EW coupling $\alpha$ with a running strong coupling $\alpha_s$. In order to end up with a final result that is free of infrared (IR) divergences, unresolved real radiation from the production and decay parts of the process need to be managed separately in the DPA and combined consistently within the employed subtraction scheme, in order to have

(i) the correct matching between subtraction counterterms and the corresponding integrated ones, and
(ii) the cancellation of IR poles between the integrated counterterms and the virtual matrix element.

In particular, gluon radiation from the W-boson decay products and from the WZ-pair-production process are treated separately within the DPA. In our calculation, we employ the dipole subtraction scheme [94–96]. For additional technical details, we refer to Ref. [28].

### B. Monte Carlo tools and input parameters

The presented SM calculation has been performed with two independent in-house multichannel Monte Carlo codes, MoCaNLO and BBMC. MoCaNLO has been recently employed for NLO EW and QCD corrections to processes with polarized EW bosons in the fully leptonic decay channel [26–28]. BBMC has been used for NLO corrections to off-shell diboson production [57–59,97] and has been modified to enable the treatment of resonances in the DPA. The UV-renormalized tree-level and one-loop SM amplitudes are provided to both codes by RECOLA [98,99]. The tensor reduction and integration of loop integrals is performed with COLLIER [100].

The calculation is carried out in the SM at NLO QCD accuracy. The five-flavor scheme and no quark-family mixing (unit CKM matrix) are understood. All light quarks and leptons are considered massless. The pole masses ($M_V$) and widths ($\Gamma_V$) of the EW bosons are calculated from the on-shell values ($M_V^{\rm OS}, \Gamma_V^{\rm OS}$) [101],

$$\begin{aligned} M_{\rm W}^{\rm OS} &= 80.379\ {\rm GeV}, & \Gamma_{\rm W}^{\rm OS} &= 2.085\ {\rm GeV}, \\ M_{\rm Z}^{\rm OS} &= 91.1876\ {\rm GeV}, & \Gamma_{\rm Z}^{\rm OS} &= 2.4952\ {\rm GeV}, \end{aligned} \quad (2)$$

according to the relations [102]

$$\begin{aligned} M_V &= \frac{M_V^{\rm OS}}{\sqrt{1+\left(\Gamma_V^{\rm OS}/M_V^{\rm OS}\right)^2}}, \\ \Gamma_V &= \frac{\Gamma_V^{\rm OS}}{\sqrt{1+\left(\Gamma_V^{\rm OS}/M_V^{\rm OS}\right)^2}}. \end{aligned} \quad (3)$$

The EW coupling $\alpha$ is calculated in the $G_\mu$ scheme [85], i.e., as a function of the Fermi constant $G_\mu$ and the weak-boson pole masses:

$$\begin{aligned} \alpha &= \frac{\sqrt{2}}{\pi} G_\mu M_{\rm W}^2 \left(1 - \frac{M_{\rm W}^2}{M_{\rm Z}^2}\right), \\ G_\mu &= 1.16638 \times 10^{-5}\ {\rm GeV}^{-2}. \end{aligned} \quad (4)$$

Since we only consider NLO QCD corrections, the masses of the top quark and of the Higgs boson do not enter the calculation. We use `NNPDF31_nlo_as_0118` [103,104] parton-distribution functions (PDFs), provided to the Monte Carlo codes via the LHAPDF interface [105]. Also the running of the strong coupling constant $\alpha_s$ is evaluated with built-in LHAPDF routines. The dipole formalism [94–96] is used for the subtraction of IR singularities of QCD origin. The $\overline{\rm MS}$ factorization scheme is employed for the treatment of initial-state collinear singularities. The central factorization and renormalization scales are both set to the same dynamical value $\mu_{\rm F} = \mu_{\rm R} = \mu_0$ (defined in Sec. II C), and the QCD-scale uncertainties are estimated with independent 7-point variations of $\mu_{\rm F}$ and $\mu_{\rm R}$, i.e., via the maxima and minima of the corresponding observables for the scale choices

$$\begin{aligned} (\mu_{\rm R}/\mu_0, \mu_{\rm F}/\mu_0) = {} & (1/2,1/2), (1/2,1), (1,1/2), \\ & (1,1), (1,2), (2,1), (2,2). \end{aligned}$$

### C. Kinematic setups and scale definition

The event selection and reconstruction are inspired by the recent CMS analysis presented in Ref. [54] (see Table 1 therein). The clustering of jets is carried out with the anti-$k_{\rm T}$ algorithm [106] recombining only partons with a rapidity smaller than 5. Two different event topologies are considered: *resolved* and *unresolved*. In the resolved topology we ask for:

(i) at least two jets (clustered with $R_0 = 0.4$) with $p_{\rm T,j} > 30$ GeV, $|y_{\rm j}| < 2.4$ and $\Delta R_{{\rm j}\ell^\pm} > 0.4$, the two jets with a pair invariant mass closest to $M_{\rm W}$ being selected as *decay jets*,
(ii) the system of the two decay jets with $p_{\rm T,jj} > 200$ GeV and $65\ {\rm GeV} < M_{\rm jj} < 105$ GeV, and
(iii) two opposite-sign, same-flavor leptons with $p_{{\rm T},\ell^\pm} > 40$ GeV, $|y_{\ell^\pm}| < 2.4$, $p_{{\rm T},\ell\ell} > 200$ GeV, and $76\ {\rm GeV} < M_{\ell\ell} < 106$ GeV.

In the unresolved topology we ask for:

(i) at least one jet (clustered with $R_0 = 0.8$) with $|y_{\rm J}| < 2.4$, $\Delta R_{{\rm J}\ell^\pm} > 0.8$, $p_{\rm T,J} > 200$ GeV and $65\ {\rm GeV} < M_{\rm J} < 105$ GeV, and
(ii) two opposite-sign, same-flavor leptons with $p_{{\rm T},\ell^\pm} > 40$ GeV, $|y_{\ell^\pm}| < 2.4$, $p_{{\rm T},\ell\ell} > 200$ GeV and $76\ {\rm GeV} < M_{\ell\ell} < 106$ .

By requiring large transverse momenta for the vector bosons, we select a boosted regime. We do not apply any veto on additional jets, as the logarithmically enhanced soft-boson radiation in real contributions [67,107,108] is suppressed thanks to the tight transverse-momentum cuts on the two bosons ($p_{{\rm T},\ell\ell} > 200$ GeV and $p_{{\rm T,J/jj}} > 200$ GeV),

avoiding huge QCD $K$-factors. Note, however, that the application of symmetric transverse-momentum cuts on the two bosons leads to very large corrections in transverse-momentum distributions close to the cut, due to the sensitivity to quasisoft and quasicollinear QCD initial-state radiation [109–113]. The central renormalization and factorization scales are set to,

$$\mu_R = \mu_F = \frac{M_{T,Z} + M_{T,J}}{2}. \tag{5}$$

The transverse masses are calculated as,

$$M_{T,Z} = \sqrt{p_{T,\ell\ell}^2 + M_{\ell\ell}^2}, \qquad M_{T,J} = \sqrt{p_{T,J}^2 + M_J^2}, \tag{6}$$

where $p_{T,J}$ and $M_J$ are, respectively, the transverse momentum and invariant mass of the hadronic system J that is identified as the decay-jet system (resolved topology) or as the hardest-$p_T$ fat jet (unresolved topology).

As previously stated, the polarization states of intermediate gauge bosons are defined in the c.m. frame, i.e., the rest frame of the system formed by the two leptons and the decay products of the W boson, which are identified for each contribution in the DPA. This choice enables for qualitative comparisons with phenomenological studies of ZW production in the fully leptonic decay channel [27,29].

### D. Validation

The independent implementation in MoCaNLO and BBMC of the general methods described in Ref. [28] has enabled validation checks at several levels of the calculation.

#### 1. Renormalization and phase-space integration

Detailed comparisons have been performed both for individual phase-space points for Born-level, virtual and real-radiation contributions, giving excellent agreement both for the QCD-scale and matrix-element evaluation. The UV finiteness of virtual amplitudes in the presence of polarized intermediate bosons has been checked varying by several orders of magnitude the UV-scale regulator as input parameter for RECOLA. Note that both codes make use of RECOLA as amplitude provider, which has been successfully compared earlier to other one-loop providers for unpolarized vector-boson pair production processes [114] and to an independent in-house code for WZ production with leptonic decays [59]. In addition, we have performed a check of the finite part of virtual QCD corrections to $q_u\bar{q}_d \to e^+e^- q_u'\bar{q}_d'$, comparing the RECOLA results against a stand-alone version of MadLoop [115]. A point-wise agreement at the $10^{-7}$ level was found for a number of phase-space points populating both the bulk and far off-shell regions of the fiducial volume.

The correct application of selection cuts (after jet clustering) in the two setups described in Sec. II C has been validated comparing results from MoCaNLO and BBMC for each $n$-body and $(n+1)$-body contribution to the cross section separately. This has been done both for the unpolarized and the polarized process, finding agreement within Monte Carlo uncertainties in all cases.

#### 2. Subtraction of IR singularities

The correct subtraction of IR singularities of QCD origin has been tested in depth, with both comparisons between the two codes and internal checks in each code separately. The dipole-subtraction kernels and the kinematics used to evaluate them has been tested for a number of individual phase-space points, finding good agreement between the two codes. This is especially relevant for subtraction dipoles associated to decay subprocess (gluon radiation off the W decay), whose kinematics has to undergo first the DPA$^{(3,2)}$ on-shell projection and second the final-state–final-state Catani–Seymour mapping [28]. Analogous checks have been performed on integrated subtraction counterterms, finding also excellent agreement for each phase-space point considered. The proper cancellation of IR poles in the sum of virtual matrix elements and $I$-operators [94] has been successfully checked varying the IR-regularization scale $\mu_{IR}$ up and down by 4 orders of magnitude about the scale defined in Eq. (5), finding independence of the result from $\mu_{IR}$ within the errors of the Monte Carlo integration. The functioning of the subtraction scheme in the DPA has been also tested by means of the technical parameters $\{\alpha_{dip}\}$ that set the integration boundaries for the radiation phase space in each dipole [116]. Varying such parameters between 1 and $10^{-2}$, has enabled to check that the sum of subtracted-real and integrated-counterterm contributions is independent of the choice of $\{\alpha_{dip}\}$ within integration uncertainties. The independence of the NLO corrections from the unphysical parameters $\mu_{IR}$ and $\{\alpha_{dip}\}$ represents a strong check given the different treatment of real radiation from the production and decay subprocess matrix elements and subtraction counterterms in the DPA. This further confirms that the methods introduced in Ref. [28] provide NLO predictions that are well under control from the IR-subtraction point of view.

#### 3. Treatment of polarizations

The definition of polarization vectors in the c.m. reference frame represents a crucial step in the calculation, especially for what concerns real radiation. Detailed checks at the phase-space-point level have been done in the Lorentz frame where polarizations are defined in the case of real corrections to the production and decay subprocesses. A complete comparison between MoCaNLO and BBMC has been performed for each contribution to the cross section, for all doubly polarized states, giving excellent agreement within integration errors for both integrated result and differential distributions (bin by bin). Further tests have been carried

TABLE I. Integrated cross sections (in fb) in the resolved and unresolved fiducial setups described in Sec. II C for unpolarized and doubly polarized $ZW^+$ production in the semileptonic decay channel. Polarizations are defined in the diboson c.m. frame. Numerical errors (in parentheses) and QCD-scale uncertainties from 7-point scale variations (in percentages) are shown. The fractions (in percentage) are computed as ratios of polarized cross sections over the unpolarized one. $K$-factors are defined as ratios of the NLO QCD cross sections with ($K_{\rm NLO}$) and without ($K_{\rm NLO}^{(\rm no\,g)}$) gluon-induced contributions over the LO ones.

| State | $\sigma_{\rm LO}$ [fb] | $f_{\rm LO}$ [%] | $\sigma_{\rm NLO}$ [fb] | $f_{\rm NLO}$ [%] | $K_{\rm NLO}$ | $K_{\rm NLO}^{(\rm no\,g)}$ |
|---|---|---|---|---|---|---|
| Resolved, $Z(e^+e^-)W^+(jj)$ | | | | | | |
| Unpolarized | $1.8567(2)^{+1.2\%}_{-1.4\%}$ | 100 | $3.036(2)^{+6.8\%}_{-5.3\%}$ | 100 | 1.635 | 1.033 |
| $Z_LW_L^+$ | $0.64603(5)^{+0.2\%}_{-0.6\%}$ | 34.8 | $0.6127(4)^{+0.9\%}_{-0.7\%}$ | 20.2 | 0.948 | 1.031 |
| $Z_LW_T^+$ | $0.08687(1)^{+0.2\%}_{-0.6\%}$ | 4.7 | $0.17012(6)^{+8.6\%}_{-6.8\%}$ | 5.6 | 1.958 | 0.967 |
| $Z_TW_L^+$ | $0.08710(1)^{+0.1\%}_{-0.6\%}$ | 4.7 | $0.24307(7)^{+10.2\%}_{-8.2\%}$ | 8.0 | 2.791 | 1.017 |
| $Z_TW_T^+$ | $0.97678(7)^{+2.0\%}_{-2.2\%}$ | 52.6 | $2.0008(7)^{+8.9\%}_{-7.1\%}$ | 65.8 | 2.048 | 1.059 |
| Interference | 0.0595(1) | 3.2 | 0.009(2) | 0.4 | | |
| Unresolved, $Z(e^+e^-)W^+(J)$ | | | | | | |
| Unpolarized | $1.6879(2)^{+1.9\%}_{-2.1\%}$ | 100 | $3.112(2)^{+7.6\%}_{-6.1\%}$ | 100 | 1.843 | 1.193 |
| $Z_LW_L^+$ | $0.61653(5)^{+1.0\%}_{-1.3\%}$ | 36.5 | $0.6799(5)^{+0.9\%}_{-0.7\%}$ | 21.9 | 1.103 | 1.170 |
| $Z_LW_T^+$ | $0.06444(1)^{+0.7\%}_{-1.0\%}$ | 3.8 | $0.17584(6)^{+10.8\%}_{-8.6\%}$ | 5.7 | 2.729 | 1.158 |
| $Z_TW_L^+$ | $0.07437(1)^{+0.6\%}_{-0.9\%}$ | 4.4 | $0.24742(8)^{+11.0\%}_{-8.9\%}$ | 8.0 | 3.327 | 1.193 |
| $Z_TW_T^+$ | $0.88233(9)^{+2.9\%}_{-2.9\%}$ | 52.3 | $2.0041(8)^{+9.6\%}_{-7.7\%}$ | 64.3 | 2.271 | 1.227 |
| Interference | 0.0503(3) | 3.0 | 0.004(2) | 0.1 | | |

out comparing the two codes for a different definition of polarization, i.e., in the laboratory frame, finding also agreement.

## III. RESULTS

In this section we present numerical results at integrated and differential level for doubly polarized and unpolarized $ZW^+$ production at the LHC in the semileptonic channel. All results shown have been obtained with MoCaNLO. We have considered the specific case of an electron-positron pair ($\ell = e$). The sum over light lepton flavors ($\ell = e, \mu$) can be simply obtained upon multiplying all cross sections by a factor of two.

### A. Integrated results

In Table I we present integrated cross sections for different polarization states in the two setups introduced in Sec. II C.

Before analyzing the QCD corrections, we focus on the LO picture that is already interesting. The contribution of the LL polarization state is rather large (≈35%) besides a sizeable TT contribution (≈50%, dominated by left–right configurations), while the contribution of the mixed polarization states is at the 10% level. The suppression of the mixed modes results from the transverse momentum cuts on the produced vector bosons of 200 GeV and the unitarity suppression of the corresponding cross sections with the square of the energy of the longitudinal vector bosons [117,118]. At variance with ZZ production, the LL signal is not suppressed owing to the triple-gauge-boson coupling that contributes to LO diagrams. At high energies, the two longitudinal bosons behave in fact like would-be Goldstone bosons [119,120] that result from an $s$-channel $W^+$ boson carrying the whole partonic energy (which exceeds 400 GeV in our setups). While in the resolved topologies the mixed polarization states have similar cross sections, in the unresolved topology the TL cross section is 15% larger than the LT one. This is due to the fact that the two quarks from the decay of a transverse W boson are preferably produced in and opposite to the direction of the W boson in the W-boson c.m. frame. Thus, they are roughly back to back in the laboratory frame and less likely recombined to a fat jet. Therefore, the two-light-jet requirement is fulfilled more easily than the requirement of a single fat jet with a mass close to $M_{\rm W}$. The decay jets of a longitudinal W boson, on the other hand, are preferably perpendicular to its direction and consequently more collinear in the laboratory frame and more likely to be recombined to a fat jet.

The overall picture at NLO QCD shows a smaller difference between the results in the two setups, especially in the case of LT and TL polarizations. The NLO QCD corrections are very large for polarization states with at least one transverse boson, with a size that is comparable to the one for the LO cross section. On the contrary, the corrections are small for the purely longitudinal state. The LL state receives negative corrections (about −5%) in

the resolved topologies, while in the unresolved setup the corrections become positive (10%). In the resolved topology the TT and LT states receive comparable corrections at the +100% level, while a different behavior between the two is found in the unresolved setup. The largest corrections in both setups (about +200%) characterize the TL polarization state. In general (both for polarized and unpolarized states), these big corrections are caused by hard QCD radiation in partonic processes with initial-state gluons [107], which are enhanced by the large gluon luminosity in the proton. In fact, omitting the gluon-induced channels, the $K$-factors are much smaller (see column labelled $K_{\mathrm{NLO}}^{(\mathrm{no\,g})}$ in Table I).

For the LL polarization state, not only the gluon-emission real corrections are small but also the gluon-induced ones (with quark emission) do not give large contributions, as already seen in inclusive ZW calculations with leptonic decays [27,29]. This can be understood as follows. As demonstrated in Ref. [108] the dominant NLO QCD corrections arise for the production of a vector-boson–quark pair in gluon-quark scattering with subsequent radiation of a soft vector boson from the quark (see also Fig. 2). However, the subprocess $\mathrm{g}q \to Vq'$ is suppressed for longitudinal high-energy vector bosons, as can seen via the Goldstone-boson equivalence theorem and the absence of LO diagrams for the corresponding process with the vector boson replaced by a would-be Goldstone boson (for massless quarks).

The striking difference (in both setups) between TL and LT at NLO QCD results from hard QCD radiation in gluon-induced partonic channels which enhances the mixed state with a longitudinal W boson much more than the one with a transverse W boson. This is a consequence of the unitarity cancellations for mixed polarization states with high transverse momenta of the longitudinal vector bosons, which also holds in the presence of additional real QCD radiation. Owing to this suppression of high-energy longitudinal bosons, kinematic configurations are preferred, where the transverse boson recoils against the longitudinal one and the additional jet, favoring (in the gluon-induced processes) configurations with a rather collimated system

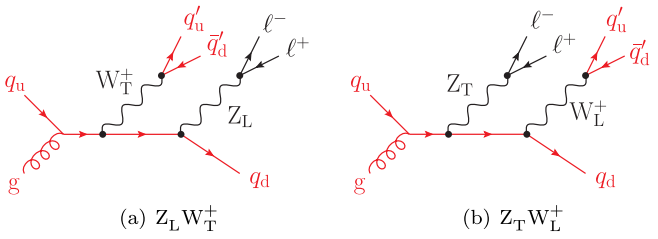


FIG. 2. Leading QCD-radiation contributions in the $q_{\mathrm{u}}\mathrm{g}$ partonic channel for longitudinal-transverse and transverse-longitudinal $\mathrm{ZW}^+$ production at the LHC in the semileptonic decay channel. Particles carrying color charge are highlighted in red.

of the longitudinal boson and the radiation jet. We have verified that the Monte Carlo integration channels corresponding to the diagrams in Figs. 2(a) and 2(b) give indeed the leading contribution to the LT and TL state, respectively. In the TL polarization mode, all jets are thus produced relatively close in phase space, resulting in a less efficient decay-jet identification. In addition, the transverse Z boson absorbs the entire hadronic recoil in the final state, allowing for a softer longitudinal boson and therefore a less severe unitarity suppression. For the LT mode the leptonically decaying longitudinal Z boson needs a transverse momentum above 200 GeV, which causes a stronger unitarity cancellation. These effects are further confirmed at differential level, as shown in Sec. III B. Up to these differences, the mixed states give a contribution of about 14% to the total cross section at NLO QCD.

The QCD correction to the TT state is similar in the two setups, giving a NLO cross section that represents 65% of the total. It is worth recalling that the ZW TT state is characterized by an approximate amplitude zero at tree level [118], which is spoiled by QCD radiation from higher orders (already at NLO).

The interference effects, obtained subtracting the sum of polarized cross sections from the unpolarized one, contribute +3% at LO and are almost negligible ($< 0.5\%$) at NLO QCD, with irrelevant differences between the two setups. This effect is more sizeable in differential results.

As expected in general for purely EW processes, the QCD-scale uncertainties at LO are small since they only come from factorization-scale variations. In addition, the requirement of the boosted regime reduces them roughly by a factor of 4 with respect to inclusive calculations [27,29]. We have checked numerically that the same effect is also found in the fully leptonic channel for the WZ process. At NLO QCD the renormalization-scale dependence of the strong coupling and the sizeable real corrections render the scale uncertainties much larger than at LO, ranging between 7% and 11% for polarization modes with at least one transverse boson. A different behavior is found for the LL mode, for which the real corrections are small and therefore the NLO QCD scale uncertainty is of the same order of magnitude as at LO (1%). The difference in scale uncertainties between the two setups is motivated by the small differences in the applied kinematic selections. Owing to the EW character of the LO ZW process, a truly NLO QCD scale dependence of the polarized cross section can only be obtained upon including NNLO QCD corrections, which is possible with the tools developed in Ref. [31]. Notice that this would also provide more reliable scale uncertainties.

The obtained results (in both setups) understand a hard cut on the transverse momentum of both bosons, which acts like a veto on additional QCD jets. Although this prevents huge QCD $K$-factors, the symmetric character of such

TABLE II. Integrated cross sections (in fb) in the resolved setup described in Sec. II C without the minimum $p_{T,jj}$ cut of 200 GeV. Polarizations are defined in the diboson c.m. frame. Numerical errors (in parentheses) and QCD-scale uncertainties from 7-point scale variations (in percentages) are shown. The fractions (in percentage) are computed as ratios of polarized cross sections over the unpolarized one. $K$-factors are defined as ratios of the NLO QCD cross sections with ($K_{NLO}$) and without ($K_{NLO}^{(no\,g)}$) gluon-induced contributions over the LO ones.

| State | $\sigma_{LO}$ [fb] | $f_{LO}$ [%] | $\sigma_{NLO}$ [fb] | $f_{NLO}$ [%] | $K_{NLO}$ | $K_{NLO}^{(no\,g)}$ |
|---|---|---|---|---|---|---|
| Resolved (no minimum $p_{T,jj}$ cut), $Z(e^+e^-)W^+(jj)$ | | | | | | |
| Unpolarized | $1.8564(1)^{+1.2\%}_{-1.4\%}$ | 100 | $5.5388(8)^{+10.6\%}_{-8.6\%}$ | 100 | 2.984 | 1.371 |
| $Z_L W_L^+$ | $0.64605(3)^{+0.2\%}_{-0.6\%}$ | 34.8 | $0.7525(4)^{+1.5\%}_{-1.2\%}$ | 13.6 | 1.165 | 1.194 |
| $Z_L W_T^+$ | $0.08687(1)^{+0.2\%}_{-0.6\%}$ | 4.7 | $0.3057(1)^{+11.4\%}_{-9.2\%}$ | 5.5 | 3.519 | 1.462 |
| $Z_T W_L^+$ | $0.08710(1)^{+0.1\%}_{-0.6\%}$ | 4.7 | $1.0486(1)^{+14.6\%}_{-11.9\%}$ | 18.9 | 12.04 | 2.408 |
| $Z_T W_T^+$ | $0.97677(7)^{+2.0\%}_{-2.2\%}$ | 52.6 | $3.5506(9)^{+11.8\%}_{-9.6\%}$ | 64.1 | 3.635 | 1.424 |
| Interference | 0.0595(1) | 3.2 | −0.119(2) | −2.1 | | |

selections ($p_{T,jj/J} > 200$ GeV, $p_{T,\ell\ell} > 200$ GeV) induces large unphysical NLO corrections in kinematic regions close to the cut [113]. These can be avoided by omitting the cut $p_{T,jj/J} > 200$ GeV. The corresponding results for the resolved setup described in Sec. II C without this cut are shown in Table II. While the LO picture is identical to the original setup, the omission of the $p_{T,jj/J}$ cut induces huge QCD corrections owing to the fact that the large transverse momentum of the leptonic system is now absorbed by the entire hadronic system, including both decay and extra real radiation jets. This leads to much larger $K$-factors for all polarization states with at least one transverse boson, while the LL contribution does not change so much, confirming the arguments given above. The QCD corrections and, in particular, the gluon-induced contributions are huge for the TL state, giving a TL component that amounts at almost 19% of the total unpolarized result (compared to 5% at LO). As expected, the TL contribution is much larger than the LT one at NLO QCD, because the Z boson is boosted ($p_{T,\ell\ell} > 200$ GeV) while the hadronically decaying W boson is not necessarily boosted, therefore the unitarity suppression is strong for the LT state but much smaller for the TL state. Note that the strong increase of the mixed polarization states is again dominantly due to the gluon-induced channels, as can be seen by inspecting the $K$-factors $K_{NLO}^{(no\,g)}$ without these contributions in Table II. Despite the small QCD corrections, the LL fraction is diminished (13.6%) with respect to the default setups (20%), but remains sizeable compared to the 6% found in inclusive fiducial setups [27,29].

We summarize the main results for fiducial $ZW^+$ cross sections in the boosted setups considered in this paper. With about 35% of the total, the LL polarization state gives a pretty large contribution at LO to the $ZW^+$ process, while it gets suppressed to about 20% when including NLO QCD corrections. This is related to the fact that the NLO QCD corrections are small for the LL final state, while they are large if at least one transverse vector boson is present. The corrections are largest in the case of one longitudinal W boson and a transverse Z boson. The impact of interferences between longitudinal and transverse polarizations is below 0.5% for the NLO QCD results. Omitting the cut $p_{T,jj/J} > 200$ GeV, the NLO QCD corrections to polarized signals with transverse Z bosons are strongly enhanced.

As a last comment of this section, we report on a LO study we performed to give a rough estimate of the most relevant irreducible backgrounds to resonant $ZW^+$ production in the $e^+e^-jj$ final state. Two more resonant structures contribute, namely $ZW^-$ and ZZ production, which have been computed with the DPA technique described in Sec. II A. The sum of the $ZW^+$, $ZW^-$, and ZZ resonant processes gives the dominant contribution to the full off-shell process at order $\mathcal{O}(\alpha^4)$, up to nonresonant effects beyond the DPA. The same final state also receives contributions of QCD type, formally of order $\mathcal{O}(\alpha_s^2\alpha^2)$ (pure QCD background) and $\mathcal{O}(\alpha_s\alpha^3)$ (QCD–EW interference), involving a Z boson decaying leptonically and two QCD-originated jets. The LO cross sections for such backgrounds are shown in Table III, for both setups introduced in Sec. II C. The resonant $ZW^-$ and ZZ processes turn out to be roughly of the same size as the unpolarized $ZW^+$ signal, with a ZZ contribution that is even larger than $ZW^+$ in the resolved setup. This hierarchy is inverted in the unresolved setup, thanks to kinematic selections that cut away more effectively the ZZ background. The effects beyond the DPA, estimated as the difference between the full off-shell EW result and the sum of the three DPA results, are at the 2%–4% level, as expected from the formal DPA accuracy of $\mathcal{O}(\Gamma_V/M_V)$. The pure-QCD nonresonant background has a severe impact on the cross section, being 20(15)-times larger than the EW result in the resolved(unresolved) setup. The interference contribution is negative but much smaller than the pure-QCD one, with a size about 6% of the full EW cross section. As already mentioned in Sec. II, in polarization analyses it is crucial to keep under control and possibly subtract all

TABLE III. Integrated LO cross sections (in fb) in the resolved and unresolved fiducial setups described in Sec. II C for: the signal process (DPA $ZW^+$), the background processes with a resonant $W^-$ boson (DPA $ZW^-$) and with two resonant Z bosons (DPA ZZ), the full off-shell process at the three perturbative orders in $\alpha_s$. The result dubbed DPA $ZV$ is understood as the sum of the three DPA contributions ($ZW^+ + ZW^- + ZZ$).

| | Resolved | | Unresolved | |
|---|---|---|---|---|
| Process | $\sigma_{LO}$ [fb] | Ratio over full $O(\alpha^4)$ | $\sigma_{LO}$ [fb] | Ratio over full $O(\alpha^4)$ |
| DPA $ZW^+$ | $1.8567(2)^{+1.2\%}_{-1.4\%}$ | 0.353 | $1.6879(2)^{+1.9\%}_{-2.1\%}$ | 0.425 |
| DPA $ZW^-$ | $1.0527(1)^{+1.3\%}_{-1.6\%}$ | 0.200 | $0.9003(1)^{+2.0\%}_{-2.1\%}$ | 0.227 |
| DPA ZZ | $2.1430(3)^{+1.3\%}_{-1.6\%}$ | 0.408 | $1.2804(2)^{+2.6\%}_{-2.7\%}$ | 0.323 |
| DPA $ZV$ | $5.0523(4)^{+1.3\%}_{-1.5\%}$ | 0.961 | $3.8685(3)^{+2.2\%}_{-2.3\%}$ | 0.975 |
| Full $O(\alpha^4)$ | $5.253(1)^{+1.2\%}_{-1.5\%}$ | 1.000 | $3.967(2)^{+2.1\%}_{-2.3\%}$ | 1.000 |
| Full $O(\alpha_s\alpha^3)$ | $-0.3124(6)^{+9.2\%}_{-10.7\%}$ | −0.059 | $-0.2145(6)^{+9.7\%}_{-11.4\%}$ | −0.054 |
| Full $O(\alpha_s^2\alpha^2)$ | $97.91(7)^{+24.3\%}_{-18.4\%}$ | 18.638 | $62.55(7)^{+25.0\%}_{-18.8\%}$ | 15.768 |

nonresonant backgrounds, especially if their size is larger than the targeted signal, e.g., QCD multijet production. We stress again that, although they are part of the same full off-shell EW signal, the three diboson processes $ZW^+$, $ZW^-$ and ZZ are characterized by very different resonance and spin structures, with LO suppressions in different polarization states and/or in different kinematic regions. Therefore, including the three of them in the same polarization analysis could end up in washing out spin-specific details in differential distributions and covering new-physics effects affecting a specific resonant process with spurious effects originated from other SM processes. In the light of extracting doubly polarized $ZW^+$ production from LHC data in the semileptonic channel, it is then crucial to subtract all of the mentioned backgrounds before further splitting the unpolarized $ZW^+$ signal into polarized subsignals.

### B. Differential results

In order to understand the relative importance of the various polarization states and the differences between the two setups at LO and at NLO QCD, it is essential to analyze differential distributions, which are presented in this section. Unless otherwise stated, the two default setups described in Sec. II C are understood.

#### 1. Distributions in the decay angles and the scattering angle

We start the discussion on differential results with the angular observable that is directly related to the polarization state of an EW boson. The polar decay angle of the lepton $e^\pm$ is defined as the angular separation between the lepton direction in the rest frame of the leptonically decaying boson ($\vec{p}^{\,*}_{e^\pm}$) and the direction of the same boson calculated in the reconstructed diboson c.m. frame ($\vec{p}^{\,c.m.}_{e^+e^-}$),

$$\cos\theta^{*,c.m.}_{e^\pm} = \frac{\vec{p}^{\,*}_{e^\pm}\cdot\vec{p}^{\,c.m.}_{e^+e^-}}{|\vec{p}^{\,*}_{e^\pm}||\vec{p}^{\,c.m.}_{e^+e^-}|}. \tag{7}$$

The differential cross section with respect to $\cos\theta^{*,c.m.}_{e^+}$ is depicted in Fig. 3. The polar decay angle $\theta^{*,c.m.}_{e^+}$ is very well suited for the discrimination between polarizations states of the Z boson, while it cannot give access to the polarization state of the other boson, therefore very similar shapes are expected for LL and LT modes, as well as for the TL and TT ones. The slight differences are a consequence of the (small) interference and spin-correlation effects. As expected from results in the fully leptonic decay channel [27,29], a longitudinally polarized Z boson gives leptons produced mostly around $\theta^{*,c.m.}_{e^+} = \pi/2$, while a transverse one populates more regions around $\cos\theta^{*,c.m.}_{e^+} = \pm 0.6$. In both cases the collinear and anticollinear configurations are suppressed by the transverse-momentum cut on the charged leptons. The NLO QCD corrections distort the polarized and unpolarized shapes only in less-populated regions. In the rest of the spectrum they give rather flat enhancements to the LL and LT distributions, while for the TT and TL states the $K$-factors mildly diminish toward positive $\cos\theta^{*,c.m.}_{e^+}$. In the regions where the TT and TL distributions feature a sharp drop, the interferences reach the 9% level at LO, while they almost disappear at NLO QCD. Overall, the leptonic decay of the Z boson is only indirectly affected by QCD effects. The results for this observables are basically identical in the two setups.

In Fig. 4 the differential cross section in the cosine of the scattering angle is shown. This angle is defined as

$$\cos\theta_{scatt} = \frac{|p^{c.m.}_{e^+e^-,z}|}{|\vec{p}^{\,c.m.}_{e^+e^-}|}, \tag{8}$$

where $\vec{p}^{\,c.m.}_{e^+e^-}$ is the three momentum of the electron–positron pair in the reconstructed diboson c.m. frame and $p^{c.m.}_{e^+e^-,z}$ is its component in the $\hat{z}$ direction. This observable is directly related to the production level, while it is expected to be rather decay agnostic, up to small effects due to the decay-product reconstruction. In Fig. 4, manifest differences can be seen for various polarization modes. At large $\cos\theta_{scatt}$

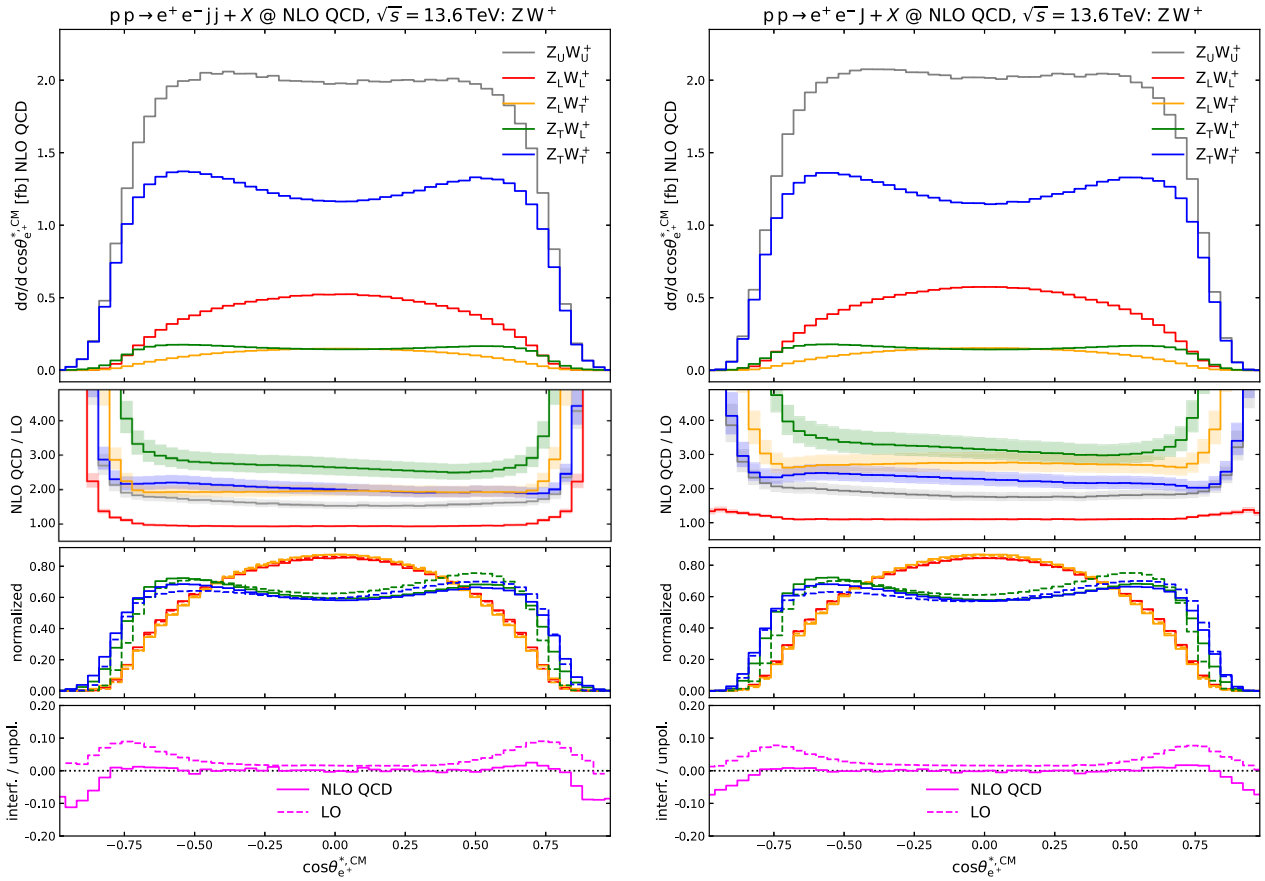


(a) Resolved topology (b) Unresolved topology

FIG. 3. Distribution in the cosine of the polar decay angle of the positron in semileptonic $ZW^+$ production at the LHC. The definition of this angle is given in Eq. (7). Results for the unpolarized and doubly polarized process are shown in the resolved (left) and unresolved (right) setups described in Sec. II C. From top down: NLO QCD differential cross sections, ratios of NLO QCD cross sections over the LO ones, normalized LO (dashed) and NLO QCD (solid) shapes (unit integral), interference contributions relative to the unpolarized cross section.

the cross section is dominated by the TT polarized state, while around zero the LL and the TT states give almost the same contribution to the unpolarized result. The QCD corrections sizeably distort the shapes of the LT, TL, and TT distributions, with a particularly significant effect in the TT case. The marked shape change for the TT state is determined by the steeply increasing $K$-factor at low $\cos\theta_{\text{scatt}}$. This is caused by real corrections spoiling the approximate amplitude-zero effect which is present at LO in the quark–antiquark annihilation into WZ [55,118]. Very large $K$-factors are also found for the LT and TL polarization modes in forward-scattering regions, where the LO signals are suppressed by unitarity cancellations due to the large transverse-momentum cuts applied on the two bosons, requiring very high scattering energy when combined with forward/backward scattering angles. All $K$-factors around $\cos\theta_{\text{scatt}} = 1$ become huge, because real radiation leaves room to configurations where the boson trajectory is closer to the beam direction, without being cut away by the rapidity selections or suppressed. Interferences at NLO QCD are almost vanishing in the most populated region, while they become non-negligible in forward-scattering configurations. The discrimination power of this angular variable among the polarization states is marked. However, using this observable is well motivated only for SM studies and measurements, since the model independence of the polarized shapes is not given. In fact, at variance with decay angles, the distribution shapes in the scattering angle could vary sizeably depending on the production dynamics, i.e., it is very sensitive to new-physics effects at production level.

### 2. Rapidity distributions

In Fig. 5 the differential cross section in the rapidity of the hadronic system J [defined after Eq. (6)] is considered. In the case where both bosons are transversely polarized the NLO QCD corrections significantly change the shape of the distribution. This is caused by the large contributions from real emission via gluon-induced processes, which mostly fill the central region, while at LO the distributions is

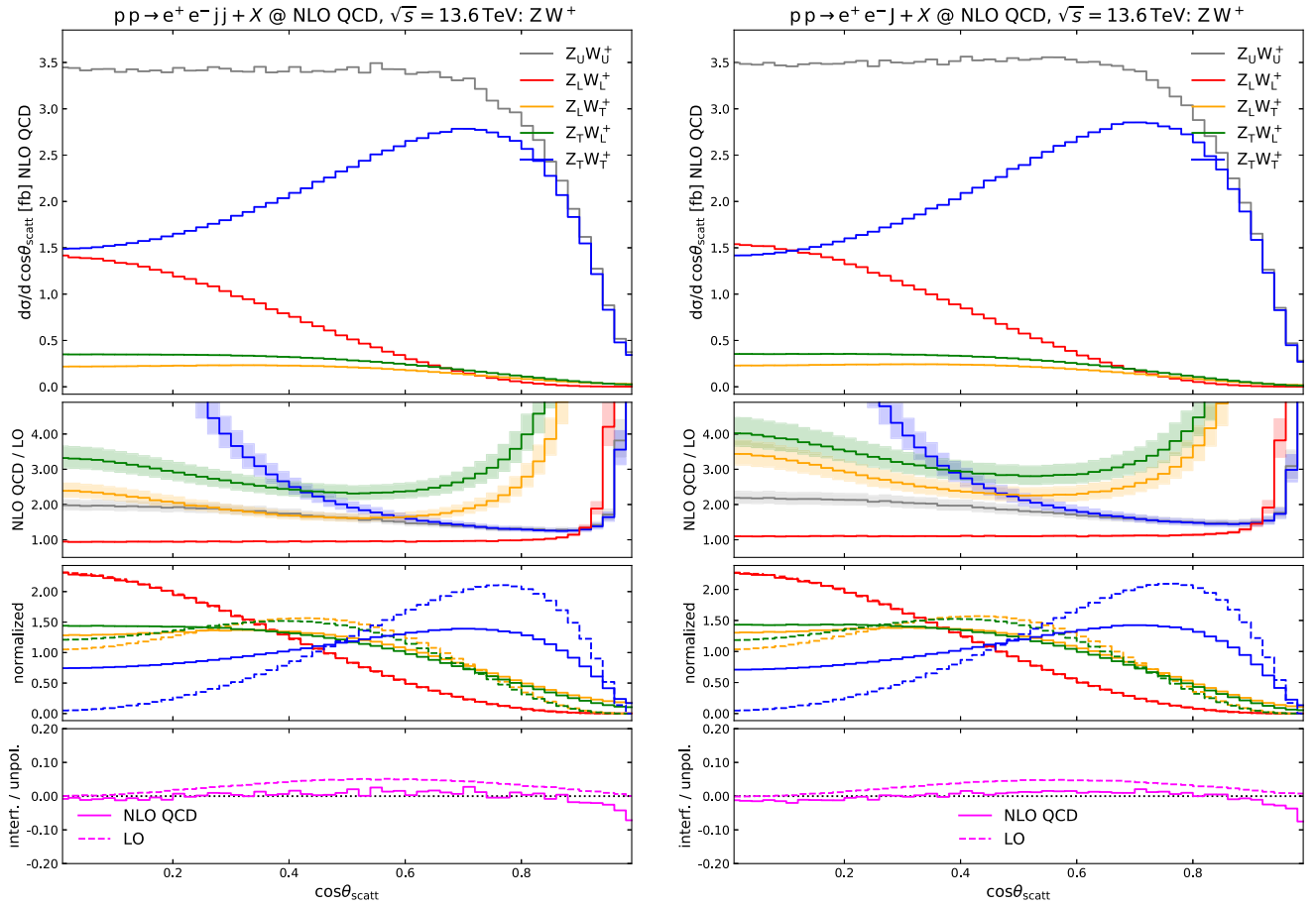


(a) Resolved topology (b) Unresolved topology

FIG. 4. Distribution in the cosine of the scattering angle in semileptonic $ZW^+$ production at the LHC. The scattering angle is defined according to Eq. (8). Same structure as Fig. 3.

almost flat for $|y_J| < 1.8$. This is an indirect effect of the approximate amplitude zero at LO, as already observed in Fig. 4 for the distributions in the scattering angle. In the resolved setup, large flat corrections are found for the TL and LT contributions, with mild nonflat effects just around $|y_J| = 2$. In the unresolved setup, the mixed states are characterized by less flat $K$-factors, giving slightly more sizable shape changes than in the resolved case. In both setups, the LL distribution only receives small corrections reflecting the result at integrated level. The interferences at NLO QCD are very small in the whole accessible spectrum, and negligible in the unresolved setup. Overall, the different shapes in the two setups are due to the sharp cut $|y_J| < 2.4$ in unresolved topologies, which is replaced in the resolved ones by rapidity cuts on single jets that suppress the region $|y_{jj}| \gtrsim 2.4$. This causes the steeper fall off at the edges of the distribution of the resolved setup compared to the unresolved setup.

In Fig. 6 the distribution in the rapidity of the electron–positron pair is presented. This observable is strongly correlated to the rapidity of the hadronic system J discussed in Fig. 5. In fact, the Z-boson momentum absorbs the recoil of the entire hadronic system, including the W boson and additional QCD radiation. Very small shape modifications are found comparing LO and NLO QCD distributions. In fact, a nonflat behavior of the $K$-factors is only found in the largest-rapidity regions that are not forbidden by selection cuts, with a mild increase toward $|y_{e^+e^-}| = 2.4$ for the TL state, a mild decrease in the same region for the LT and TT states. Up to different overall normalizations, the corrections behave very similarly in the two setups. The shapes for different polarization states are very close to each other. Only in the central region the TT component is slightly more peaked than the others. Interference contributions are basically independent of $y_{e^+e^-}$.

The distribution shown in Fig. 7 concerns the absolute value of the rapidity difference between the positron and the hadronic system J. Similarly to the scattering angle, this observable is well suited to discriminate among different polarization states, thanks to the marked shape differences. Concerning model dependence, the same caveats apply as for the distribution in the scattering angle. The LL, the TL,

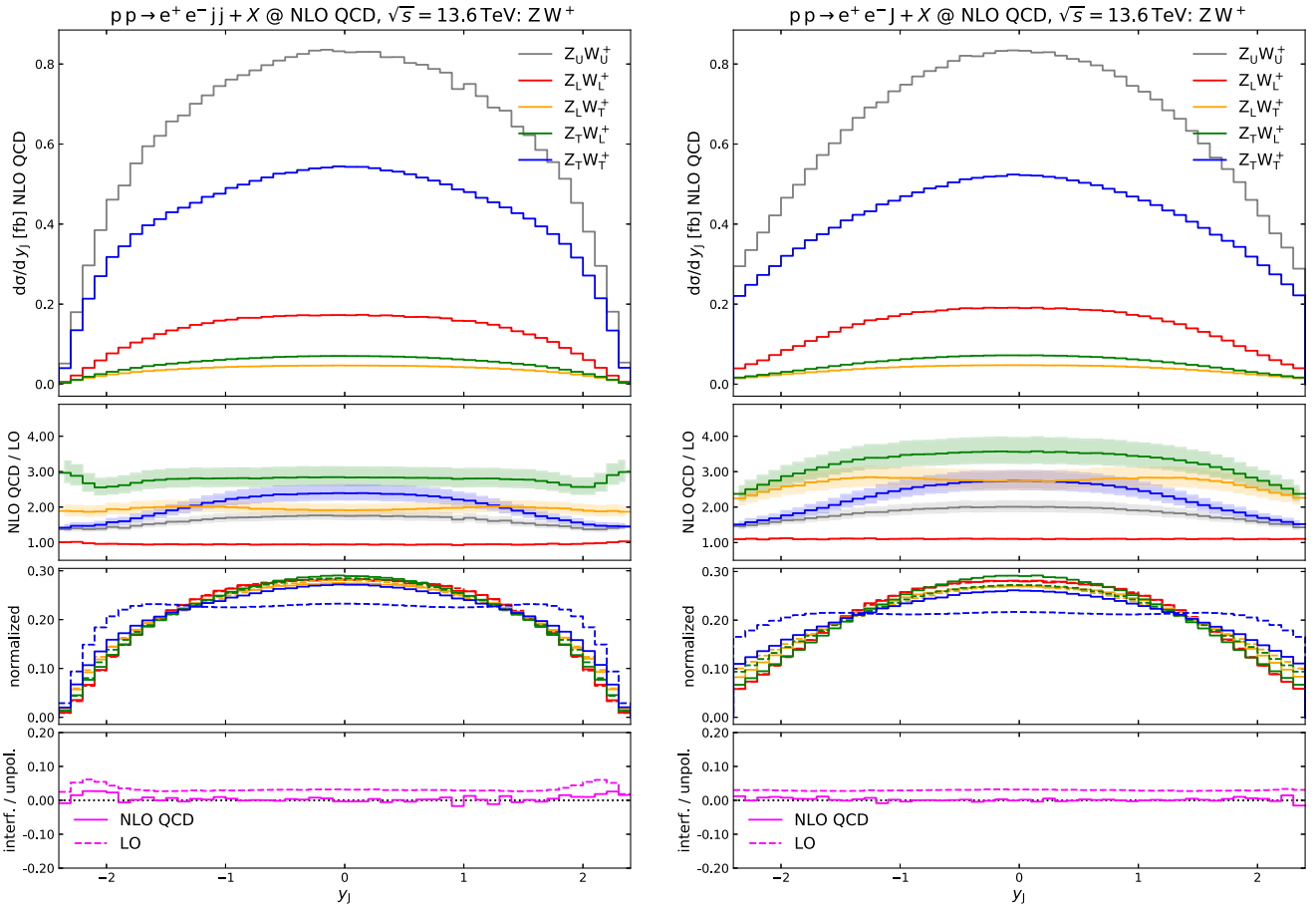


(a) Resolved topology (b) Unresolved topology

FIG. 5. Rapidity distribution of the hadronic system J in semileptonic $ZW^+$ production at the LHC. The identification of the hadronic system J is described in Sec. II C. Same structure as Fig. 3.

and the LT polarization states have a maximum at $|\Delta y_{e^+J}| = 0$, while the maximum of the TT state is shifted to $|\Delta y_{e^+J}| \approx 0.65$. The LO TT shape is heavily distorted by QCD corrections, again due to real radiation that fills kinematic regions that are suppressed at LO due to the approximate amplitude zero ($|\Delta y_{e^+J}| \approx 0$). The LT and TL polarization states receive large and increasing corrections from real radiation in gluon-induced channels for $|\Delta y_{e^+J}| \gtrsim 2.5$, where the LO is extremely suppressed. In general, at large rapidity separation all signals are suppressed by the rapidity cuts. Interferences are very small through the whole spectrum at NLO QCD. Apart from different total cross sections, the two kinematic setups give almost identical results for all polarization states, both in terms of normalized shapes and in terms of $K$-factor behaviors.

### 3. Invariant-mass distributions

Although the angular observables are the most promising ones in terms of the discrimination power among polarization states, it is important to complement their investigation with the study of energy-dependent observables. In Fig. 8 we show differential results in the invariant mass of the hadronic system J. While the distributions feature, as expected, the Breit–Wigner shape of the W-boson resonance, this observable is heavily affected by the reconstruction of the hadronic decay and therefore subject to contamination from QCD radiation. In fact, the NLO QCD real corrections introduce an ambiguity in the determination of the $W^+$-boson decay jets. The jets that happen to be part of the reconstructed hadronic system J without being actual decay products of the $W^+$ boson create a background that does not follow the Breit–Wigner modulation. This effect is particularly manifest in the TL distribution. When the recombined W boson becomes off-shell, the TL curve does not fall off like the others (and in particular the LT one, which is almost identical at LO), but rather results in a much flatter behavior. The striking difference between the TL and LT states, beyond the different overall normalization that has already been motivated in Sec. III A, is due to the interplay

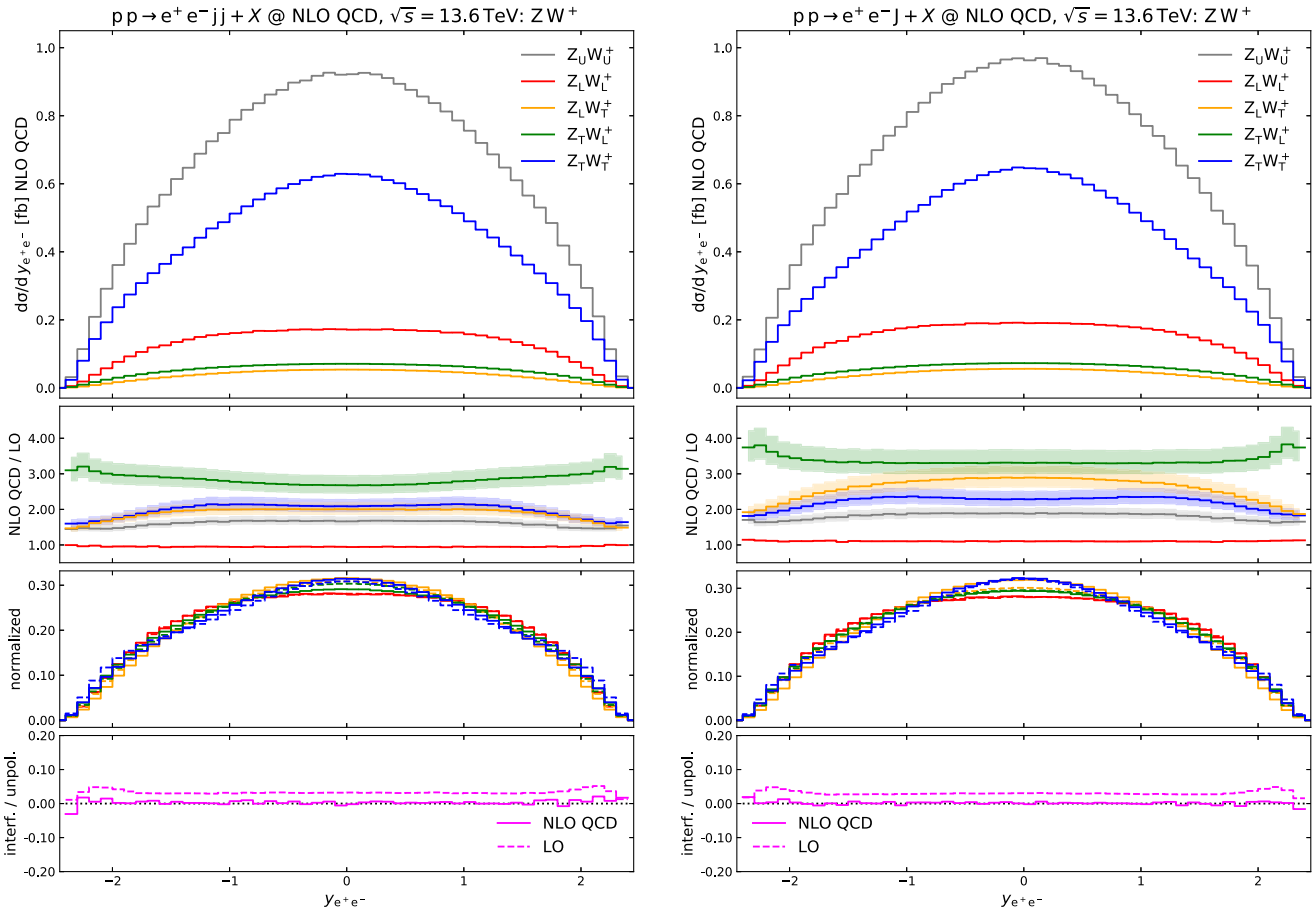


(a) Resolved topology (b) Unresolved topology

FIG. 6. Rapidity distribution of the electron-positron pair in semileptonic $ZW^+$ production at the LHC. Same structure as Fig. 3.

between the reconstruction of the hadronic system and the suppression of longitudinal bosons in mixed polarization states in the high-energy regime. In particular, both states are unitarity suppressed at LO (as can be easily seen upon replacement of the longitudinal boson with the corresponding would-be Goldstone boson), while at NLO QCD there is an enhancement due to the opening of the gluon-(anti)quark channel that gives a sizeable real correction. As discussed in Sec. III A, for the LT polarization state the bremsstrahlung parton is produced preferably opposite to the direction of the hadronically decaying W boson. Therefore little ambiguity is left for the assignment of decay jets to the transverse W boson. In the TL case, on the other hand, the additional parton is produced close to the longitudinal, hadronically decaying W boson. This deteriorates the reconstruction of the W decay products and results in a distorted shape with a Breit–Wigner peak (events with correct assignment, lower in shape compared to the LT state) on top of a sizeable flat background (events with wrong assignment). This feature originates from the hard $p_T$ cut that is applied to the hadronically decaying W boson, vetoing effectively jets with soft and moderate transverse momentum.

We have checked that without the hard $p_T$ requirement on the hadronic system J the shape of the TL distribution is closer to the others, as can be appreciated in Fig. 9(a) where we consider the resolved setup as in Fig. 8(a) but without the $p_{T,jj} > 200$ GeV cut. The assignment of decay jets to the W boson, although not perfect, behaves much better for the TL mode, further confirming the reasoning above and in particular the correlation between the flat background from misreconstruction and the high-$p_{T,J}$ cut. The absence of a hard transverse-momentum cut on the hadronic decay system J leads to abundant real QCD radiation filling the pure radiative region below 100 GeV for the leading decay jet, which is excluded at LO by the required $p_T$ of the Z boson, as can be observed in the distribution in the $p_T$ of the hardest jet from the W-boson decay shown in Fig. 9(b). The distribution for the TL mode exhibits a clear peak around 50 GeV, while a hard cut $p_{T,jj} > 200$ GeV would remove all events with $p_{T,j_1} < 100$ GeV. The same effect is present also for the LT and TT polarized states, but

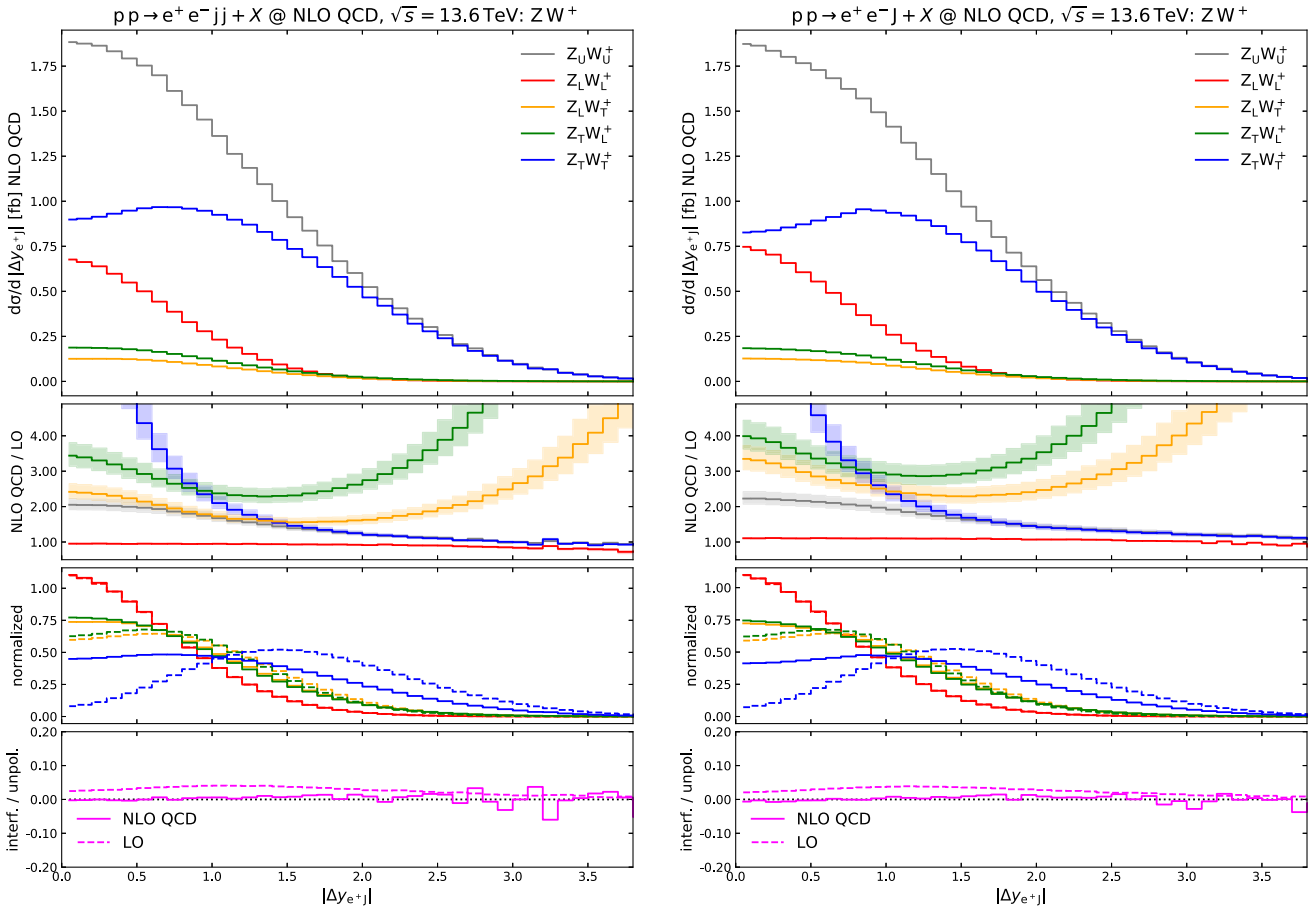


(a) Resolved topology (b) Unresolved topology

FIG. 7. Distribution in the rapidity separation between the positron and the hadronic system J in semileptonic $ZW^+$ production at the LHC. The identification of the hadronic system J is described in Sec. II C. Same structure as Fig. 3.

much less pronounced. The interference contribution is a the level of 10% for $p_{T,J} < 100$ GeV.

Coming back to the results in the default setups shown in Fig. 8, the differences in the TL distribution between the resolved and unresolved topology are due to the effects of the clustering algorithms on the reconstruction procedure. In particular, the flat background from misreconstruction of the W-boson decay jets is larger (giving a normalized shape with a lower peak) in the unresolved setup, because the larger recombination radius causes more initial-state QCD radiation fall in the decay-jet system. Looking at Fig. 8, the TT and LT distributions feature very similar shapes when going far from the on-shell regime, since the QCD effects do not depend much on the polarization mode of the leptonic Z boson, apart from the different normalization determined by the unitarity suppression of the longitudinal polarization. The LL state is characterized by QCD $K$-factors that are below one at the peak, while they are monotonically increasing in off-shell regimes. In the resolved setup, the corrections increase faster for $M_J < M_W$, resulting from events where one of the decay jets is missed in the reconstruction of the W boson, while in the unresolved one the corrections are larger for $M_J > M_W$, indicating an initial-state-radiation jet be clustered together with one of the decay jets. This is a direct consequence of the more inclusive jet clustering in the unresolved setup. For the TT, LT, and LL states the omission of the $p_{T,jj}$ cut does not change the general picture, apart from the different normalization.

In Fig. 10 the differential cross section is presented with respect to the invariant mass of the hadronic system J and the positron. Large differences among various polarization states occur. The low-invariant-mass regime ($M_{e^+J} < 200$ GeV) is dominated by real-emission contributions. In fact, the additional QCD jet allows for the Z and $W^+$ bosons to be produced with a lower boson-pair invariant mass. The larger jet-recombination radius in the unresolved setup leads to higher $M_{e^+J}$ thus suppressing the contributions in the low-invariant-mass region. At large $M_{e^+J}$ the TT distribution falls off slower than all the others. In the resolved setup the LL distribution becomes lower than the TL one around 900 GeV, while in the unresolved setup the LL signal remains larger than TL, with similar

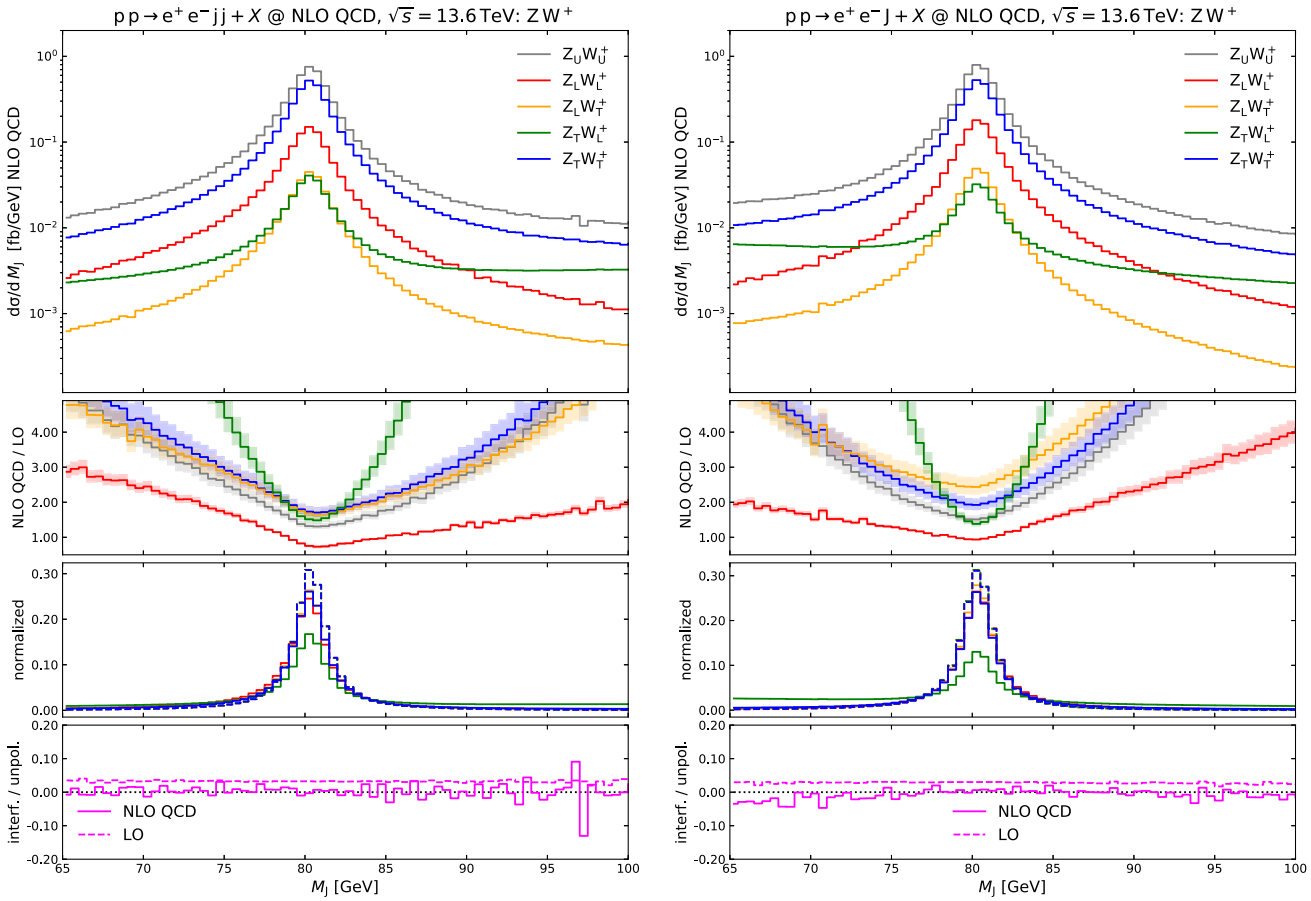


(a) Resolved topology (b) Unresolved topology

FIG. 8. Invariant-mass distribution of the hadronic system J in semileptonic $ZW^+$ production at the LHC. The identification of the hadronic system J is described in Sec. II C. Same structure as Fig. 3.

suppressions at high energy. The much stronger suppression of the LL state in the resolved setup leads to a signal that is almost one order of magnitude smaller than in the unresolved case at 1 TeV. This is due to the fact that for the LL state the high partonic energy is shared between the two bosons (effect of additional radiation is small for the LL state) resulting in LO-like configurations with two collimated quarks that are easily clustered together. This clearly disfavors the resolved topologies where two jets are required. Rather large negative interferences are present in the radiation-driven soft part of the spectrum at NLO ($\approx -10\%$). Shape-wise the LL distribution features a pronounced peak around 400 GeV, while the other polarization states, and especially the TT one, are more spread over the shown spectrum.

#### 4. Transverse-momentum distributions

Similar features are found in transverse-momentum distributions for the positron, which are shown in Fig. 11. The behavior in the low transverse-momentum region strongly depends on the polarization of the Z boson (of which the positron is a decay product) and affects the normalized shapes. For a transverse (longitudinal) Z boson the shape has a local minimum (maximum) around $p_{T,e^+} \approx 130$ GeV. This is due explained looking at Fig. 3(a): a transverse polarization gives a positively charged lepton that goes more frequently in the same or opposite direction with respect to the Z boson, therefore sharing in a nondemocratic way the boson energy (two peaks at $p_{T,e^+} \approx 20$ GeV and $p_{T,e^+} \approx 200$ GeV), while a longitudinal one gives leptons that are preferably orthogonal to the boson trajectory and share democratically the boson energy (single peak at $p_{T,e^+} \approx 130$ GeV). The marked shape differences and the small interference effects for $p_{T,e^+} \lesssim 200$ GeV, namely in the most-populated region, makes this transverse-momentum observable suitable for the discrimination of the Z-boson polarization state. Another interesting aspect of the results is the slower fall-off of the distributions in the unresolved setup compared to the resolved setup, which is particularly significant for the double-longitudinal signal. This is the same effect as observed in Fig. 10 for the invariant mass of the positron–jet

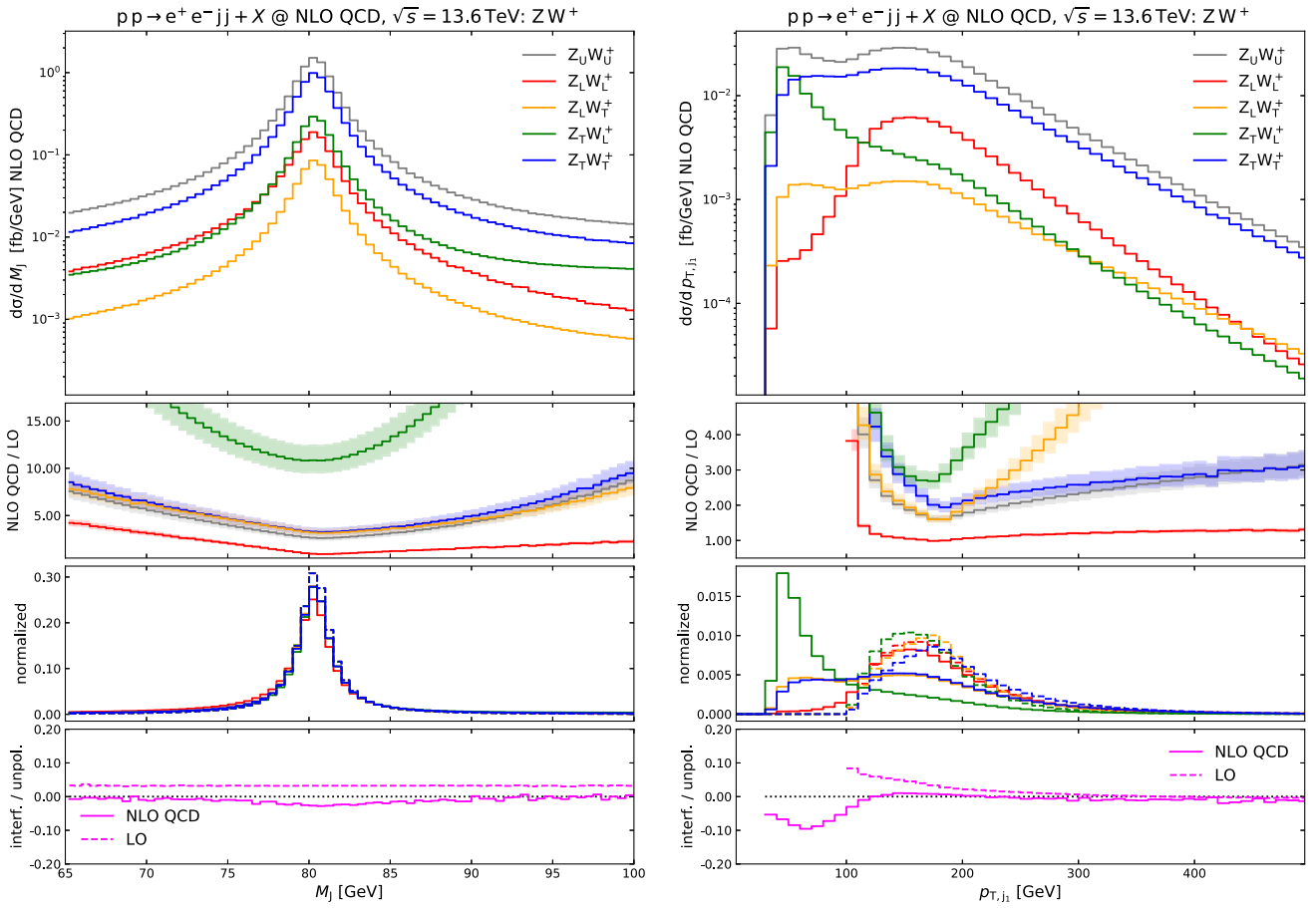


(a) $M_{\mathrm{J}}$ (b) $p_{\mathrm{T,j_1}}$

FIG. 9. Distribution in the invariant mass of the hadronic system J (a) and in the transverse momentum of the hardest decay jet (b) in semileptonic $ZW^+$ production at the LHC. The identification of the hadronic system J is described in Sec. II C. The resolved setup is considered, but no minimum cut is applied on $p_{\mathrm{T,jj}}$. The panels of the subfigures have the same structure as in Fig. 3.

system, which is highly correlated to the transverse momentum of the positron. For $p_{\mathrm{T,e^+}} \gtrsim 300$ GeV, all $K$-factors increase faster in the resolved topology compared to the unresolved one, owing to a different LO suppression. Requiring at least two jets in the final state results in high-$p_{\mathrm{T}}$ events being cut away at LO, as the almost collinear decay quarks are often clustered into a single jet. In the unresolved topology such events are not discarded (at least one fat jet is required). Since the two vector bosons are produced with opposite transverse momenta, the same effects are found in the high-energy tails of the transverse-momentum distributions for the hadronic system J, the Z boson, and the charged leptons.

### 5. Distributions depending on individual decay jets in the resolved topology

In the resolved topology it is possible to distinguish the two jets that come from the W-boson decay, up to potentially relevant reconstruction effects. In Fig. 12 we consider two observables that depend on the kinematics of individual jets (those labeled as decay jets, sorted according to their transverse momentum). The polar decay angle of the leading decay jet $\mathrm{j_1}$ in Fig. 12(a) is defined similarly to the one of the charged lepton in Eq. (7): it is the angular separation between the leading-jet direction in the rest frame of the hadronic system J ($\vec{p}^{\,*}_{\mathrm{j_1}}$) and the direction of J calculated in the reconstructed diboson c.m. frame ($\vec{p}^{\,c.m.}_{\mathrm{J}}$),

$$\cos\theta^{*,c.m.}_{\mathrm{j_1}} = \frac{\vec{p}^{\,*}_{\mathrm{j_1}} \cdot \vec{p}^{\,c.m.}_{\mathrm{J}}}{|\vec{p}^{\,*}_{\mathrm{j_1}}||\vec{p}^{\,c.m.}_{\mathrm{J}}|}. \tag{9}$$

Note that this observable is sensitive to the reconstruction procedure to identify the hadronic system J and is not selecting the uplike or downlike jet (which would be unphysical) but rather the leading-$p_{\mathrm{T}}$ one. At variance with the leptonic decay angle in the Z-boson rest frame, the hardest jet can originate from an up-type or a down-type quark, strongly distorting the description of the boson decay. Strikingly, all distributions are nonvanishing only between $\cos\theta^{*,c.m.}_{\mathrm{j_1}} \approx -0.4$ and $\cos\theta^{*,c.m.}_{\mathrm{j_1}} = 1$, clearly

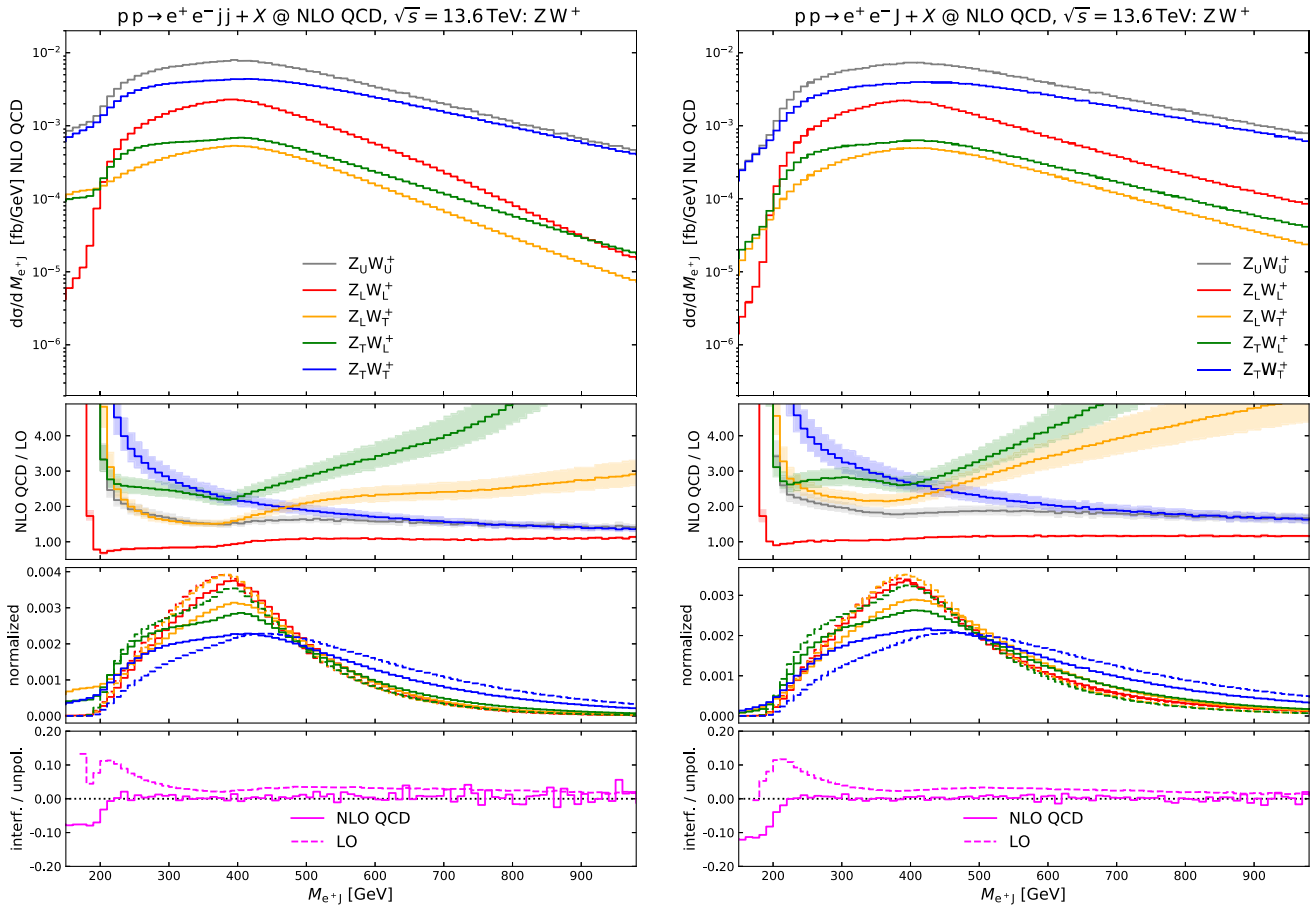


(a) Resolved topology (b) Unresolved topology

FIG. 10. Invariant-mass distributions of the system formed by the hadronic system J and the positron in semileptonic $ZW^+$ production at the LHC. The identification of the hadronic system J is described in Sec. II C. Same structure as Fig. 3.

favoring the positive region of the spectrum. In fact, the hardest jet is mostly produced in the same direction of the decayed boson, of which it takes the largest fraction of transverse momentum. The analogous distributions for the softest jet show the opposite behavior, populating mostly the negative region of the spectrum. The LO shape for the TL state follows the one of the LL state. This is expected as this angular variable is directly related to the polarization state of the W boson (and agnostic to the Z-boson one). This relation is somewhat deteriorated, compared to the decay into leptons, since the identification of the flavor and charge of individual quarks is not physical, therefore the decay jets can only be ordered according to their transverse momenta. In contrast, at NLO QCD the TL shape is following the LT and TT ones. This dramatic change in the TL shape, driven by large and nonflat real QCD corrections in gluon-induced channels, is due to the combination of the bad reconstruction of the W boson, discussed already for Figs. 8 and 9, the suppression of the LO signal, and the choice of sorting the decay jets in $p_T$. The interference effects at NLO QCD are practically negligible in the most populated region, while they increase up to more than 10% toward the endpoints of the spectrum.

In Fig. 12(b) we show the differential cross section with respect to the transverse momentum of the softest jet from the W-boson decay. As expected, all distributions decrease very fast already at moderate transverse momentum. For the LL polarization state (both at LO and at NLO) and the TL one (just at LO), the distributions are peaked around 100 GeV, namely half of the minimum transverse momentum required by the selections for the W boson. This behavior is understood as the longitudinal W boson, mostly produced at large scattering angles (see Fig. 4), favors configurations where the two decay jets are orthogonal to the boson direction (in its rest frame) and therefore typically share half of the boson transverse momentum. At NLO, the LL shape does not deviate from the LO one as the QCD corrections are very small, while the TL shape becomes peaked around zero, following closely the shape of the TT and LT distributions. This strong modification of the TL distribution is due to large effects of misreconstruction induced by real QCD radiation. In particular, the

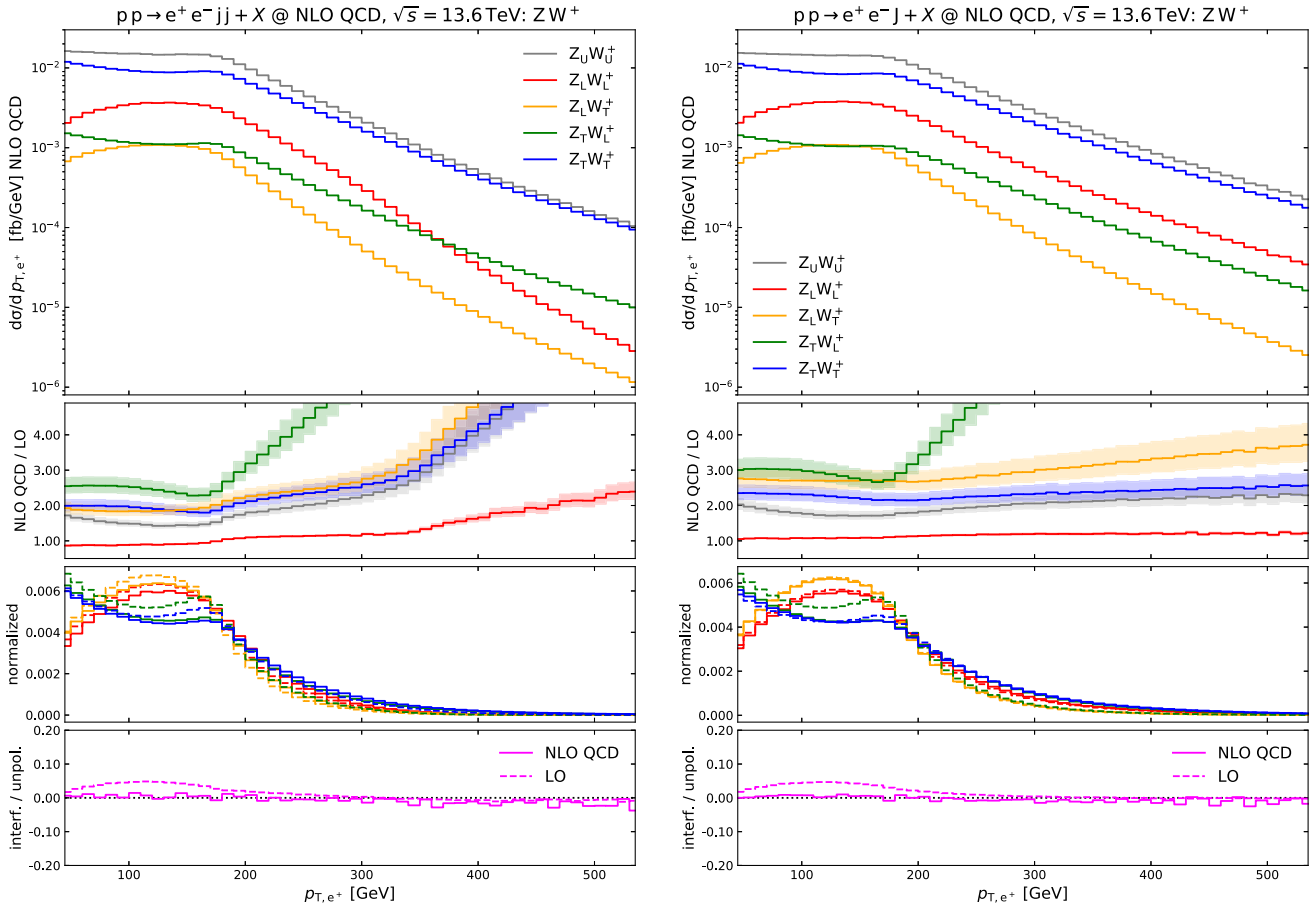


(a) Resolved (b) Unresolved topology

FIG. 11. Transverse-momentum distributions of the positron in semileptonic $ZW^+$ production at the LHC. Same structure as Fig. 3.

gluon-induced contributions that dominate the NLO QCD corrections to the TL state, shown in Fig. 2(b), prefer a boosted, transversely polarized Z boson whose recoil is absorbed by the system of a hard QCD parton and a soft pair of quarks from the longitudinal-W-boson decay. After clustering and reconstruction, this topology results in one hard jet and one soft jet, mimicking the jet pattern characteristic for the hadronic decay of a transverse W boson (TT and LT modes). The TT and LT distributions show very similar shapes, dominated by the soft region ($p_{\mathrm{T,j_1}} < 100$ GeV), while for $p_{\mathrm{T,j_1}} > 100$ GeV the QCD corrections enhance the LT signal. In fact, for transverse W bosons, one decay jet is preferably emitted opposite to the direction of the boson, resulting in a small transverse momentum of this subleading decay jet.

We summarize our main findings for distributions. On the one hand, the NLO QCD corrections to the distribution in the leptonic-decay angle of the Z boson follow closely those for the fiducial cross section with mild shape modifications. On the other hand, QCD corrections sizeably distort the shapes of the distributions in the scattering angle and in the rapidity difference between the positron and the hadronic system. The radiative corrections significantly change the shape of the rapidity distribution of the hadronic system for final states with two longitudinal vector bosons. For the TL polarization state, the NLO QCD corrections deteriorate the reconstruction of the hadronically decaying W boson resulting in a flat nonresonant background in the corresponding invariant-mass distribution, especially in the presence of a strong cut on the transverse momentum of the reconstructed W boson. The QCD corrections and their interplay with the employed reconstruction technique lead to a distortion of the distribution in the invariant mass of the positron and the hadronic system, as well as the distributions involving resolved decay jets, in particular for the TL polarization state.

Besides decay-angle distributions, also the distributions in the scattering angle and in the rapidity difference between the positron and the hadronic system are sensitive to the polarizations of the vector bosons, although the latter two are model dependent. Further distributions that are sensitive to different vector-boson polarizations are those in the transverse momentum of the positron and in the

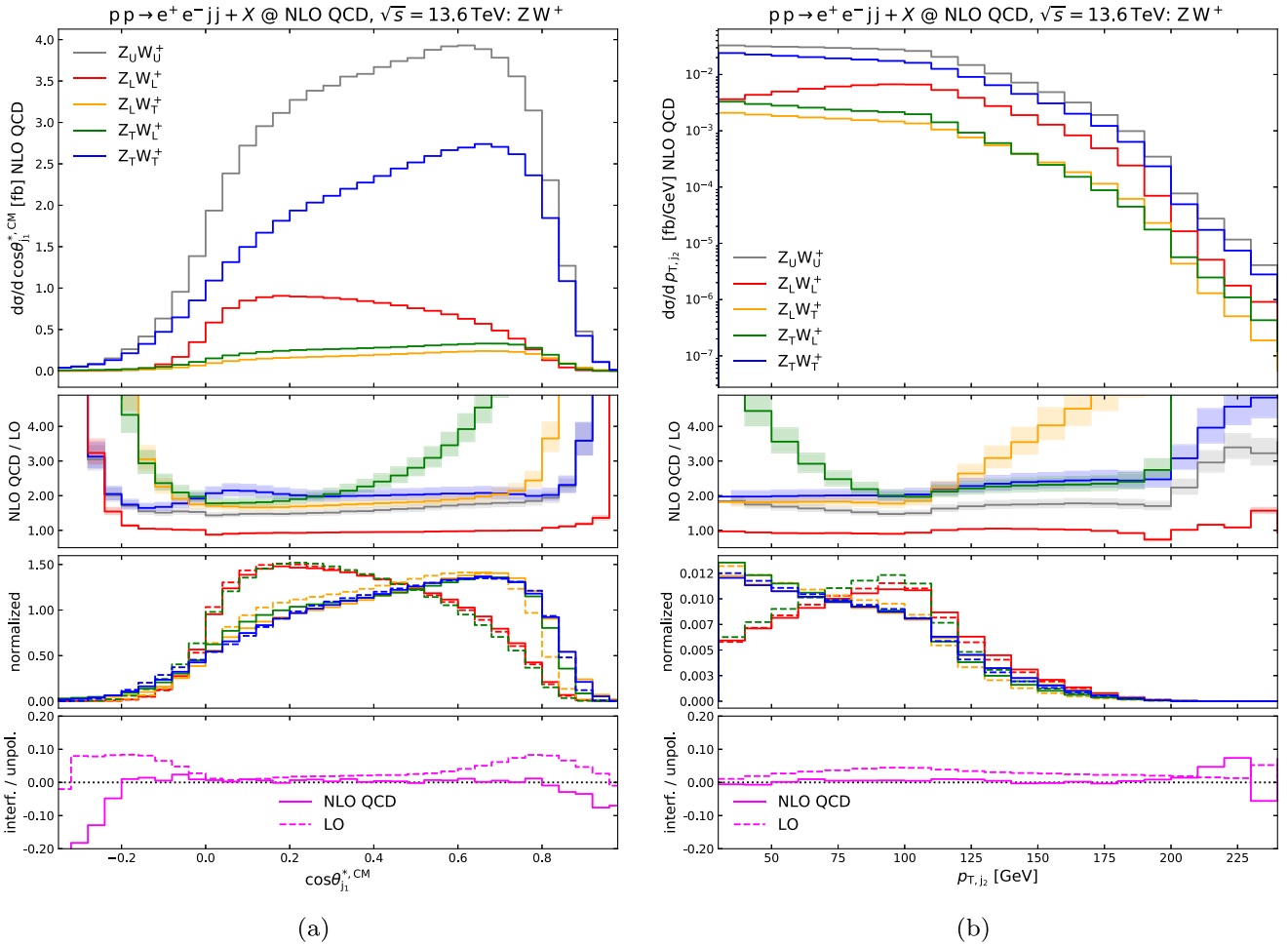


FIG. 12. Distributions in the leading-jet decay angle (left) and in the subleading-jet transverse momentum (right) in semileptonic $ZW^+$ production at the LHC. The identification of the leading and subleading jet is discussed in Sec. II C and the decay-angle definition is given in Eq. (9). Results for the unpolarized and doubly polarized process are shown in the resolved setup described in Sec. II B. The panels of the subfigures have the same structure as in Fig. 3.

invariant mass of the positron and the hadronic system. Distributions depending on the decay jets are sensitive to the polarization of the hadronically decaying W boson, although they can be heavily distorted by NLO QCD corrections. Whether the sensitivity to the polarization is still present in distributions after a parton shower matching is an open question.

## IV. CONCLUSION

In this work we have presented NLO QCD corrections to vector-boson-pair inclusive production in the semileptonic decay channel. The results focus on the WZ process in final states with two charged leptons and jets, but can be easily extended to ZZ production with the same final state, as well as to processes with a charged lepton, missing transverse momentum and jets (WZ and $W^+W^-$). The building blocks at NLO QCD are exactly the same as those used for this calculation.

Although we have neglected a number of effects, including the overlap with other production mechanisms, the nonresonant background and other sources of corrections (NLO EW, matching to parton shower), the presented calculation represents a crucial step toward precise predictions for diboson processes in semileptonic decay channels. For the first time, we have combined in the double-pole approximation the QCD corrections to the production of two bosons and to the hadronic decay of one of the two, separating doubly polarized signals at the level of tree-level and one-loop Standard Model amplitudes.

We have considered a boosted regime, where the longitudinal signals give a more sizeable contribution than in inclusive setups. We have applied two different jet selections: a first one with two light jets (resolved) and a second one with a single fat jet (unresolved). Between the two setups moderate differences show up at the level of distribution shapes and more marked deviations are revealed for QCD $K$-factors for the various polarization states.

The reconstruction of the hadronic decay of the W boson is found to behave very differently for the various polarization states, distorting angular and energy-dependent distributions and enhancing otherwise suppressed contributions. The largest impact is found when the W boson is longitudinally polarized and the leptonically decaying Z boson is transversely polarized, as a combination of unitarity cancellations and a hard cut on the transverse momentum of the longitudinal bosons. For this polarization mode, the sizeable QCD corrections and their interplay with the reconstruction procedure causes distributions for decay observables of the longitudinal W boson to mimic those of transverse bosons.

Strikingly, a number of observables turn out to be highly sensitive to polarization-state discrimination. Many of these observables are inclusive in the hadronic decay structure, i.e., they do not rely on jet-substructure techniques. This clearly suggests that extracting relevant polarization information from the data is possible even avoiding any reconstruction of the subjets from the hadronic decay. Resolving individual decay jets from the hadronic decay gives access to a larger set of distributions which are sensitive to the polarization of the decaying boson. These results demonstrate that semileptonic final states could give an important boost to the investigation of polarized diboson production, both via decay-specific analyses and as complementary to fully leptonic final states. In spite of very large backgrounds to be subtracted, the semileptonic channel would in fact enhance the sensitivity to weak-boson polarizations, otherwise restricted to fully leptonic final states, which are clean but statistically limited.

The dramatic change of (doubly) polarized distributions when going from LO to NLO QCD makes it essential to include at least NLO QCD corrections in any polarization study or data analysis in the considered decay channel. This statement, however, applies also for fully leptonic channels, as shown in previous works [26–31]. Including NLO corrections is especially important for multiboson processes that are characterized by a LO suppression in some kinematic configurations. The inclusion of NNLO QCD corrections, though definitely desirable and now feasible for diboson processes [31], is not expected to give as dramatic shape distortions to the NLO distributions, as those given by the NLO corrections to the LO shapes. With specific regards to the hadronic decays of EW bosons, it will be especially relevant to match NLO QCD (or NNLO QCD) calculations to parton showers and hadronization, enabling a realistic comparison against LHC data. It is hard to estimate the impact that the parton-shower matching will have on the sensitivity to vector-boson polarizations, although in general a deterioration could be expected owing to additional radiations coming both from the initial state and from the boson decay. A public code to match polarized-boson fixed-order calculations and parton showers is still lacking. However, since the external degrees of freedom of the matrix elements are unpolarized, even in the presence of intermediate vector bosons with fixed polarization state, we do not foresee conceptual complications in the matching of polarized fixed-order results to parton-shower effects compared to the case of unpolarized vector bosons.

## ACKNOWLEDGMENTS

The authors are grateful to Jean-Nicolas Lang for maintaining RECOLA and to Stefan Rode for testing one-loop amplitudes with intermediate polarized bosons. We would like to thank Lucia Di Ciaccio, Joany Manjarres, Mathieu Pellen, René Poncelet, Emmanuel Sauvan, and Frank Siegert for useful discussions. This work is supported by the German Federal Ministry for Education and Research (BMBF) under contract no. 05H21WWCAA and by the German Research Foundation (DFG) under reference number DFG 623/8-1.

[1] M. Aaboud *et al.* (ATLAS Collaboration), Measurement of $W^{\pm}Z$ production cross sections and gauge boson polarization in $pp$ collisions at $\sqrt{s} = 13$ TeV with the ATLAS detector, Eur. Phys. J. C **79**, 535 (2019).

[2] A. Tumasyan *et al.* (CMS Collaboration), Measurement of the inclusive and differential WZ production cross sections, polarization angles, and triple gauge couplings in pp collisions at $\sqrt{s} = 13$ TeV, J. High Energy Phys. 07 (2022) 032.

[3] ATLAS Collaboration, Observation of gauge boson joint-polarisation states in $W^{\pm}Z$ production from $pp$ collisions at $\sqrt{s} = 13$ TeV with the ATLAS detector, arXiv:2211.09435.

[4] A. M. Sirunyan *et al.* (CMS Collaboration), Measurements of production cross sections of polarized same-sign W boson pairs in association with two jets in proton-proton collisions at $\sqrt{s} = 13$ TeV, Phys. Lett. B **812**, 136018 (2021).

[5] S. Chatrchyan *et al.* (CMS Collaboration), Measurement of the Polarization of $W$ Bosons with Large Transverse Momenta in W + Jets Events at the LHC, Phys. Rev. Lett. **107**, 021802 (2011).

[6] G. Aad *et al.* (ATLAS Collaboration), Measurement of the polarisation of W bosons produced with large transverse momentum in $pp$ collisions at $\sqrt{s} = 7$ TeV with the ATLAS experiment, Eur. Phys. J. C **72**, 2001 (2012).

[7] M. Aaboud *et al.* (ATLAS Collaboration), Measurement of the W boson polarisation in $t\bar{t}$ events from pp collisions at $\sqrt{s} = 8$ TeV in the lepton + jets channel with ATLAS, Eur. Phys. J. C **77**, 264 (2017); **79**, 19(E) (2019).

[8] V. Khachatryan *et al.* (CMS Collaboration), Measurement of the W boson helicity fractions in the decays of top quark pairs to lepton + jets final states produced in pp collisions at $\sqrt{s} = 8$ TeV, Phys. Lett. B **762**, 512 (2016).

[9] V. Khachatryan *et al.* (CMS Collaboration), Angular coefficients of Z bosons produced in pp collisions at $\sqrt{s} =$ 8 TeV and decaying to $\mu^+\mu^-$ as a function of transverse momentum and rapidity, Phys. Lett. B **750**, 154 (2015).

[10] G. Aad *et al.* (ATLAS Collaboration), Measurement of the angular coefficients in Z-boson events using electron and muon pairs from data taken at $\sqrt{s} = 8$ TeV with the ATLAS detector, J. High Energy Phys. 08 (2016) 159.

[11] G. Aad *et al.* (CMS and ATLAS Collaborations), Combination of the W boson polarization measurements in top quark decays using ATLAS and CMS data at $\sqrt{s} = 8$ TeV, J. High Energy Phys. 08 (2020) 051.

[12] Z. Bern *et al.*, Left-handed $W$ bosons at the LHC, Phys. Rev. D **84**, 034008 (2011).

[13] W. J. Stirling and E. Vryonidou, Electroweak gauge boson polarisation at the LHC, J. High Energy Phys. 07 (2012) 124.

[14] R. Gauld, A. Gehrmann-De Ridder, T. Gehrmann, E. W. N. Glover, and A. Huss, Precise predictions for the angular coefficients in Z-boson production at the LHC, J. High Energy Phys. 11 (2017) 003.

[15] R. Frederix and T. Vitos, Electroweak corrections to the angular coefficients in finite-$p_T$ Z-boson production and dilepton decay, Eur. Phys. J. C **80**, 939 (2020).

[16] M. Pellen, R. Poncelet, A. Popescu, and T. Vitos, Angular coefficients in $W + j$ production at the LHC with high precision, Eur. Phys. J. C **82**, 693 (2022).

[17] R. Rahaman and R. K. Singh, Anomalous triple gauge boson couplings in ZZ production at the LHC and the role of Z boson polarizations, Nucl. Phys. **B948**, 114754 (2019).

[18] R. Rahaman and R. K. Singh, Unravelling the anomalous gauge boson couplings in $ZW^{\pm}$ production at the LHC and the role of spin-1 polarizations, J. High Energy Phys. 04 (2020) 075.

[19] J. Baglio and N. Le Duc, Fiducial polarization observables in hadronic WZ production: A next-to-leading order QCD + EW study, J. High Energy Phys. 04 (2019) 065.

[20] J. Baglio and N. Le Duc, Polarization observables in WZ production at the 13 TeV LHC: Inclusive case, Communications in Physics **30**, 35 (2020).

[21] R. Rahaman and R. K. Singh, Breaking down the entire spectrum of spin correlations of a pair of particles involving fermions and gauge bosons, Nucl. Phys. **B984**, 115984 (2022).

[22] A. Ballestrero, E. Maina, and G. Pelliccioli, W boson polarization in vector boson scattering at the LHC, J. High Energy Phys. 03 (2018) 170.

[23] A. Ballestrero, E. Maina, and G. Pelliccioli, Polarized vector boson scattering in the fully leptonic WZ and ZZ channels at the LHC, J. High Energy Phys. 09 (2019) 087.

[24] A. Ballestrero, E. Maina, and G. Pelliccioli, Different polarization definitions in same-sign $WW$ scattering at the LHC, Phys. Lett. B **811**, 135856 (2020).

[25] D. Buarque Franzosi, O. Mattelaer, R. Ruiz, and S. Shil, Automated predictions from polarized matrix elements, J. High Energy Phys. 04 (2020) 082.

[26] A. Denner and G. Pelliccioli, Polarized electroweak bosons in $W^+W^-$ production at the LHC including NLO QCD effects, J. High Energy Phys. 09 (2020) 164.

[27] A. Denner and G. Pelliccioli, NLO QCD predictions for doubly-polarized WZ production at the LHC, Phys. Lett. B **814**, 136107 (2021).

[28] A. Denner and G. Pelliccioli, NLO EW and QCD corrections to polarized ZZ production in the four-charged-lepton channel at the LHC, J. High Energy Phys. 10 (2021) 097.

[29] D. N. Le and J. Baglio, Doubly-polarized WZ hadronic cross sections at NLO QCD + EW accuracy, Eur. Phys. J. C **82**, 917 (2022).

[30] D. N. Le, J. Baglio, and T. N. Dao, Doubly-polarized WZ hadronic production at NLO QCD + EW: Calculation method and further results, Eur. Phys. J. C **82**, 1103 (2022).

[31] R. Poncelet and A. Popescu, NNLO QCD study of polarised $W^+W^-$ production at the LHC, J. High Energy Phys. 07 (2021) 023.

[32] E. Maina, Vector boson polarizations in the decay of the Standard Model Higgs, Phys. Lett. B **818**, 136360 (2021).

[33] E. Maina and G. Pelliccioli, Polarized Z bosons from the decay of a Higgs boson produced in association with two jets at the LHC, Eur. Phys. J. C **81**, 989 (2021).

[34] M. Pellen, R. Poncelet, and A. Popescu, Polarised W + j production at the LHC: A study at NNLO QCD accuracy, J. High Energy Phys. 02 (2022) 160.

[35] J. Searcy, L. Huang, M.-A. Pleier, and J. Zhu, Determination of the $WW$ polarization fractions in $pp \to W^{\pm}W^{\pm}jj$ using a deep machine learning technique, Phys. Rev. D **93**, 094033 (2016).

[36] J. Lee, N. Chanon, A. Levin, J. Li, M. Lu, Q. Li, and Y. Mao, Polarization fraction measurement in same-sign WW scattering using deep learning, Phys. Rev. D **99**, 033004 (2019).

[37] J. Lee, N. Chanon, A. Levin, J. Li, M. Lu, Q. Li, and Y. Mao, Polarization fraction measurement in ZZ scattering using deep learning, Phys. Rev. D **100**, 116010 (2019).

[38] M. Grossi, J. Novak, B. Kersevan, and D. Rebuzzi, Comparing traditional and deep-learning techniques of kinematic reconstruction for polarization discrimination in vector boson scattering, Eur. Phys. J. C **80**, 1144 (2020).

[39] T. Han, D. Krohn, L.-T. Wang, and W. Zhu, New physics signals in longitudinal gauge boson scattering at the LHC, J. High Energy Phys. 03 (2010) 082.

[40] A. Belyaev and D. Ross, What does the CMS measurement of W-polarization tell us about the underlying theory of the coupling of W-bosons to matter?, J. High Energy Phys. 08 (2013) 120.

[41] J. Brehmer, J. Jaeckel, and T. Plehn, Polarized WW scattering on the Higgs pole, Phys. Rev. D **90**, 054023 (2014).

[42] S. Brass, C. Fleper, W. Kilian, J. Reuter, and M. Sekulla, Transversal modes and Higgs bosons in electroweak

vector-boson scattering at the LHC, Eur. Phys. J. C **78**, 931 (2018).
[43] Q.-H. Cao, B. Yan, C. P. Yuan, and Y. Zhang, Probing $Zt\bar{t}$ couplings using $Z$ boson polarization in $ZZ$ production at hadron colliders, Phys. Rev. D **102**, 055010 (2020).
[44] S. De, V. Rentala, and W. Shepherd, Measuring the polarization of boosted, hadronic $W$ bosons with jet substructure observables, arXiv:2008.04318.
[45] T. Kim and A. Martin, A $W^{\pm}$ polarization analyzer from deep neural networks, arXiv:2102.05124.
[46] A. Dey and T. Samui, Jet substructure and multivariate analysis aid in polarization study of boosted, hadronic $W$ Fatjet at the LHC, arXiv:2110.02773.
[47] L. Ricci and M. Riembau, Energy correlators of hadronically decaying electroweak bosons, Phys. Rev. D **106**, 114010 (2022).
[48] V. Cavaliere, R. Les, T. Nitta, and K. Terashi, HE-LHC prospects for diboson resonance searches and electroweak WW/WZ production via vector boson scattering in the semi-leptonic final states, arXiv:1812.00841.
[49] J. Roloff, V. Cavaliere, M.-A. Pleier, and L. Xu, Sensitivity to longitudinal vector boson scattering in semileptonic final states at the HL-LHC, Phys. Rev. D **104**, 093002 (2021).
[50] A. M. Sirunyan *et al.* (CMS Collaboration), Search for a heavy resonance decaying into a Z boson and a Z or W boson in $2\ell 2$q final states at $\sqrt{s} = 13$ TeV, J. High Energy Phys. 09 (2018) 101.
[51] M. Aaboud *et al.* (ATLAS Collaboration), Combination of searches for heavy resonances decaying into bosonic and leptonic final states using 36 fb$^{-1}$ of proton-proton collision data at $\sqrt{s} = 13$ TeV with the ATLAS detector, Phys. Rev. D **98**, 052008 (2018).
[52] A. M. Sirunyan *et al.* (CMS Collaboration), Combination of CMS searches for heavy resonances decaying to pairs of bosons or leptons, Phys. Lett. B **798**, 134952 (2019).
[53] G. Aad *et al.* (ATLAS Collaboration), Search for heavy diboson resonances in semileptonic final states in pp collisions at $\sqrt{s} = 13$ TeV with the ATLAS detector, Eur. Phys. J. C **80**, 1165 (2020).
[54] A. Tumasyan *et al.* (CMS Collaboration), Search for heavy resonances decaying to ZZ or ZW and axion-like particles mediating nonresonant ZZ or ZH production at $\sqrt{s} = 13$ TeV, J. High Energy Phys. 04 (2022) 087.
[55] D. Liu and L.-T. Wang, Prospects for precision measurement of diboson processes in the semileptonic decay channel in future LHC runs, Phys. Rev. D **99**, 055001 (2019).
[56] S. Kallweit, J. M. Lindert, S. Pozzorini, and M. Schönherr, NLO QCD + EW predictions for $2\ell 2\nu$ diboson signatures at the LHC, J. High Energy Phys. 11 (2017) 120.
[57] B. Biedermann, M. Billoni, A. Denner, S. Dittmaier, L. Hofer, B. Jäger, and L. Salfelder, Next-to-leading-order electroweak corrections to $pp \to W^+W^- \to 4$ leptons at the LHC, J. High Energy Phys. 06 (2016) 065.
[58] B. Biedermann, A. Denner, S. Dittmaier, L. Hofer, and B. Jäger, Next-to-leading-order electroweak corrections to the production of four charged leptons at the LHC, J. High Energy Phys. 01 (2017) 033.
[59] B. Biedermann, A. Denner, and L. Hofer, Next-to-leading-order electroweak corrections to the production of three charged leptons plus missing energy at the LHC, J. High Energy Phys. 10 (2017) 043.
[60] F. Cascioli, T. Gehrmann, M. Grazzini, S. Kallweit, P. Maierhöfer, A. von Manteuffel, S. Pozzorini, D. Rathlev, L. Tancredi, and E. Weihs, ZZ production at hadron colliders in NNLO QCD, Phys. Lett. B **735**, 311 (2014).
[61] M. Grazzini, S. Kallweit, and D. Rathlev, ZZ production at the LHC: Fiducial cross sections and distributions in NNLO QCD, Phys. Lett. B **750**, 407 (2015).
[62] M. Grazzini, S. Kallweit, S. Pozzorini, D. Rathlev, and M. Wiesemann, $W^+W^-$ production at the LHC: Fiducial cross sections and distributions in NNLO QCD, J. High Energy Phys. 08 (2016) 140.
[63] M. Grazzini, S. Kallweit, D. Rathlev, and M. Wiesemann, $W^{\pm}Z$ production at hadron colliders in NNLO QCD, Phys. Lett. B **761**, 179 (2016).
[64] G. Heinrich, S. Jahn, S. P. Jones, M. Kerner, and J. Pires, NNLO predictions for Z-boson pair production at the LHC, J. High Energy Phys. 03 (2018) 142.
[65] M. Grazzini, S. Kallweit, D. Rathlev, and M. Wiesemann, $W^{\pm}Z$ production at the LHC: Fiducial cross sections and distributions in NNLO QCD, J. High Energy Phys. 05 (2017) 139.
[66] S. Kallweit and M. Wiesemann, ZZ production at the LHC: NNLO predictions for $2\ell 2\nu$ and $4\ell$ signatures, Phys. Lett. B **786**, 382 (2018).
[67] M. Grazzini, S. Kallweit, J. M. Lindert, S. Pozzorini, and M. Wiesemann, NNLO QCD + NLO EW with Matrix + OpenLoops: Precise predictions for vector-boson pair production, J. High Energy Phys. 02 (2020) 087.
[68] F. Caola, K. Melnikov, R. Röntsch, and L. Tancredi, QCD corrections to $W^+W^-$ production through gluon fusion, Phys. Lett. B **754**, 275 (2016).
[69] F. Caola, K. Melnikov, R. Röntsch, and L. Tancredi, QCD corrections to ZZ production in gluon fusion at the LHC, Phys. Rev. D **92**, 094028 (2015).
[70] M. Grazzini, S. Kallweit, M. Wiesemann, and J. Y. Yook, ZZ production at the LHC: NLO QCD corrections to the loop-induced gluon fusion channel, J. High Energy Phys. 03 (2019) 070.
[71] S. Alioli, F. Caola, G. Luisoni, and R. Röntsch, ZZ production in gluon fusion at NLO matched to parton-shower, Phys. Rev. D **95**, 034042 (2017).
[72] E. Re, M. Wiesemann, and G. Zanderighi, NNLOPS accurate predictions for $W^+W^-$ production, J. High Energy Phys. 12 (2018) 121.
[73] S. Bräuer, A. Denner, M. Pellen, M. Schönherr, and S. Schumann, Fixed-order and merged parton-shower predictions for WW and WWj production at the LHC including NLO QCD and EW corrections, J. High Energy Phys. 10 (2020) 159.
[74] M. Chiesa, C. Oleari, and E. Re, NLO QCD + NLO EW corrections to diboson production matched to parton shower, Eur. Phys. J. C **80**, 849 (2020).
[75] S. Alioli, A. Broggio, A. Gavardi, S. Kallweit, M. A. Lim, R. Nagar, and D. Napoletano, Next-to-next-to-leading order event generation for Z boson pair production

matched to parton shower, Phys. Lett. B **818**, 136380 (2021).
[76] S. Alioli, S. Ferrario Ravasio, J. M. Lindert, and R. Röntsch, Four-lepton production in gluon fusion at NLO matched to parton showers, Eur. Phys. J. C **81**, 687 (2021).
[77] J. M. Lindert, D. Lombardi, M. Wiesemann, G. Zanderighi, and S. Zanoli, $W^{\pm}Z$ production at NNLO QCD and NLO EW matched to parton showers with $\mathrm{MiNNLO_{PS}}$, J. High Energy Phys. 11 (2022) 036.
[78] S. Groote, J. G. Körner, and P. Tuvike, $O(\alpha_s)$ corrections to the decays of polarized $W^{\pm}$ and Z bosons into massive quark pairs, Eur. Phys. J. C **72**, 2177 (2012).
[79] S. Groote, J. G. Körner, and P. Tuvike, Fully analytical $\mathcal{O}(\alpha_s)$ results for on-shell and off-shell polarized W-boson decays into massive quark pairs, Eur. Phys. J. C **73**, 2454 (2013).
[80] For the pole approximation for one resonance see also Refs. [81,82].
[81] R. G. Stuart, General renormalization of the gauge invariant perturbation expansion near the $Z^0$ resonance, Phys. Lett. B **272**, 353 (1991).
[82] R. G. Stuart, Gauge invariance, analyticity and physical observables at the $Z^0$ resonance, Phys. Lett. B **262**, 113 (1991).
[83] A. Aeppli, F. Cuypers, and G. J. van Oldenborgh, O(Γ) corrections to W pair production in $e^+e^-$ and $\gamma\gamma$ collisions, Phys. Lett. B **314**, 413 (1993).
[84] A. Aeppli, G. J. van Oldenborgh, and D. Wyler, Unstable particles in one loop calculations, Nucl. Phys. **B428**, 126 (1994).
[85] A. Denner, S. Dittmaier, M. Roth, and D. Wackeroth, Electroweak radiative corrections to $e^+e^- \to WW \to 4$ fermions in double-pole approximation: The RACOONWW approach, Nucl. Phys. **B587**, 67 (2000).
[86] A. Denner, S. Dittmaier, M. Roth, and L. Wieders, Electroweak corrections to charged-current $e^+e^- \to 4$ fermion processes: Technical details and further results, Nucl. Phys. **B724**, 247 (2005); **B854**, 504(E) (2012).
[87] A. Denner and S. Dittmaier, Electroweak radiative corrections for collider physics, Phys. Rep. **864**, 1 (2020).
[88] M. Billoni, S. Dittmaier, B. Jäger, and C. Speckner, Next-to-leading order electroweak corrections to pp $\to$ $W^+W^- \to 4$ leptons at the LHC in double-pole approximation, J. High Energy Phys. 12 (2013) 043.
[89] C. Uhlemann and N. Kauer, Narrow-width approximation accuracy, Nucl. Phys. **B814**, 195 (2009).
[90] P. Artoisenet, R. Frederix, O. Mattelaer, and R. Rietkerk, Automatic spin-entangled decays of heavy resonances in Monte Carlo simulations, J. High Energy Phys. 03 (2013) 015.
[91] W. Beenakker, A. P. Chapovsky, and F. A. Berends, Non-factorizable corrections to W pair production: Methods and analytic results, Nucl. Phys. **B508**, 17 (1997).
[92] A. Denner, S. Dittmaier, and M. Roth, Non-factorizable photonic corrections to $e^+e^- \to WW \to 4$ fermions, Nucl. Phys. **B519**, 39 (1998).
[93] W. Beenakker, F. A. Berends, and A. P. Chapovsky, Radiative corrections to pair production of unstable particles: Results for $E^+E^- \to 4$ fermions, Nucl. Phys. **B548**, 3 (1999).
[94] S. Catani and M. Seymour, A general algorithm for calculating jet cross sections in NLO QCD, Nucl. Phys. **B485**, 291 (1997); **B510**, 503(E) (1998).
[95] S. Dittmaier, A general approach to photon radiation off fermions, Nucl. Phys. **B565**, 69 (2000).
[96] S. Catani, S. Dittmaier, M. H. Seymour, and Z. Trocsanyi, The dipole formalism for next-to-leading order QCD calculations with massive partons, Nucl. Phys. **B627**, 189 (2002).
[97] B. Biedermann, A. Denner, S. Dittmaier, L. Hofer, and B. Jäger, Electroweak Corrections to $pp \to \mu^+\mu^-e^+e^- + X$ at the LHC: A Higgs Background Study, Phys. Rev. Lett. **116**, 161803 (2016).
[98] S. Actis, A. Denner, L. Hofer, A. Scharf, and S. Uccirati, Recursive generation of one-loop amplitudes in the Standard Model, J. High Energy Phys. 04 (2013) 037.
[99] S. Actis, A. Denner, L. Hofer, J.-N. Lang, A. Scharf, and S. Uccirati, RECOLA: Recursive computation of one-loop amplitudes, Comput. Phys. Commun. **214**, 140 (2017).
[100] A. Denner, S. Dittmaier, and L. Hofer, COLLIER: A FORTRAN-based complex one-loop library in extended regularizations, Comput. Phys. Commun. **212**, 220 (2017).
[101] M. Tanabashi *et al.* (Particle Data Group), Review of particle physics, Phys. Rev. D **98**, 030001 (2018).
[102] D. Bardin, A. Leike, T. Riemann, and M. Sachwitz, Energy-dependent width effects in $e^+e^-$ annihilation near the Z-boson pole, Phys. Lett. B **206**, 539 (1988).
[103] R. D. Ball *et al.* (NNPDF Collaboration), Parton distributions from high-precision collider data, Eur. Phys. J. C **77**, 663 (2017).
[104] V. Bertone, S. Carrazza, N. P. Hartland, and J. Rojo (NNPDF Collaboration), Illuminating the photon content of the proton within a global PDF analysis, SciPost Phys. **5**, 008 (2018).
[105] A. Buckley, J. Ferrando, S. Lloyd, K. Nordström, B. Page, M. Rüfenacht, M. Schönherr, and G. Watt, LHAPDF6: Parton density access in the LHC precision era, Eur. Phys. J. C **75**, 132 (2015).
[106] M. Cacciari, G. P. Salam, and G. Soyez, The anti-$k_t$ jet clustering algorithm, J. High Energy Phys. 04 (2008) 063.
[107] M. Rubin, G. P. Salam, and S. Sapeta, Giant QCD K-factors beyond NLO, J. High Energy Phys. 09 (2010) 084.
[108] J. Baglio, N. Le Duc, and M. M. Weber, Massive gauge boson pair production at the LHC: A next-to-leading order story, Phys. Rev. D **88**, 113005 (2013); **94**, 099902(E) (2016).
[109] M. Klasen and G. Kramer, Dijet cross-sections at $O(\alpha\alpha_s^2)$ in photon-proton collisions, Phys. Lett. B **366**, 385 (1996).
[110] B. W. Harris and J. F. Owens, Photoproduction of jets at HERA in next-to-leading order QCD, Phys. Rev. D **56**, 4007 (1997).
[111] S. Frixione and G. Ridolfi, Jet photoproduction at HERA, Nucl. Phys. **B507**, 315 (1997).
[112] A. Denner, S. Dittmaier, S. Kallweit, and A. Mück, Electroweak corrections to Higgs-strahlung off W/Z bosons at the Tevatron and the LHC with HAWK, J. High Energy Phys. 03 (2012) 075.

[113] G. P. Salam and E. Slade, Cuts for two-body decays at colliders, J. High Energy Phys. 11 (2021) 220.
[114] J. R. Andersen *et al.*, Les Houches 2017: Physics at TeV colliders standard model working group report, arXiv: 1803.07977.
[115] V. Hirschi, R. Frederix, S. Frixione, M. V. Garzelli, F. Maltoni, and R. Pittau, Automation of one-loop QCD corrections, J. High Energy Phys. 05 (2011) 044.
[116] Z. Nagy and Z. Trocsanyi, Next-to-leading order calculation of four jet observables in electron positron annihilation, Phys. Rev. D **59**, 014020 (1999); **62**, 099902(E) (2000).
[117] S. S. D. Willenbrock, Pair production of W and Z bosons and the Goldstone boson equivalence theorem, Ann. Phys. (N.Y.) **186**, 15 (1988).
[118] U. Baur, T. Han, and J. Ohnemus, Amplitude Zeros in $W^{\pm}Z$ Production, Phys. Rev. Lett. **72**, 3941 (1994).
[119] J. M. Cornwall, D. N. Levin, and G. Tiktopoulos, Derivation of gauge invariance from high-energy unitarity bounds on the $S$ matrix, Phys. Rev. D **10**, 1145 (1974); **11**, 972(E) (1975).
[120] C. E. Vayonakis, Born helicity amplitudes and cross-sections in non-Abelian gauge theories, Lett. Nuovo Cimento **17**, 383 (1976).